Parameterization of Wind Evolution using Lidar

Yiyin Chen[1], David Schlipf[2], and Po Wen Cheng[1]

[1]Stuttgart Wind Energy (SWE) at Institute of Aircraft Design, University of Stuttgart, Allmandring 5b, 70569 Stuttgart, Germany
[2]Wind Energy Technology Institute, Flensburg University of Applied Sciences, Kanzleistraße 91-93, 24943 Flensburg, Germany

Correspondence: Yiyin Chen (chen@ifb.uni-stuttgart.de)

Abstract. Wind evolution refers to the change of the turbulence structure of the eddies over time while the eddies are advected by the main flow over space. With the development of the lidar-assisted wind turbine control, modelling of the wind evolution becomes an interesting topic, because the control system should only react to the changes in the wind field which can be predicted accurately over the distance to avoid harmful and unnecessary control action.

5   This paper aims to achieve a parameterization model for the wind evolution model to predict the wind evolution model parameters according to the wind field conditions. For this purpose, a two-parameter wind evolution model suggested in literature was applied to model the wind evolution and the wind evolution was estimated using lidar data. A statistical analysis was done to reveal the characteristics of wind evolution model parameters. Gaussian process regression was applied to achieve the parameterization model. The results have proven the applicability of Gaussian process regression model to predict the wind

10   evolution model parameters with sufficient accuracy.

1 Introduction

Wind evolution refers to the physical phenomenon that the turbulence structure of the eddies changes over time while the eddies are advected by the main flow over space. The mathematical measure of the "change" of turbulence structure is usually defined as magnitude-squared coherence (hereinafter for brevity, also referred to as coherence) between two time series data sets of

15   the turbulent velocity with certain time shift. Coherence is a dimensionless statistic in the frequency domain that can describe the correlation between two signals or data sets, taking value between 0, for no correlation, to 1.0, for perfect correlation. Whereas, Taylor's hypothesis is a special case that assumes the pattern of turbulent motion remains unchanged while the eddies are carried by the main flow (Taylor, 1938). In other words, Taylor's hypothesis assumes a perfect correlation, which means the coherence is 1.0 over the whole frequency range.

20   The research on wind evolution dates back to 1970s. Pielke and Panofsky (1970) attempted to generalize some of the mathematical description of the horizontal variation of turbulence characteristics. The final goal at that time was to figure out an empirical model of the four dimensional space-time structure of turbulence. In Pielke and Panofsky's work (1970), the coherence model suggested by Davenport (1961) to describe the correlation between horizontal wind components at different heights, also known as Davenport Geometric Similarity, was extended into other wind components and separation directions.

25   They also followed Davenport's idea to approximate the coherence with a simple exponential function with a single decay parameter, which is known as Pielke and Panofsky's model. The decay parameters were assumed to be some constants in that research. After that, Ropelewski et al. (1973) did a systematic study of the coherence for streamwise and cross-stream wind components with horizontal separations. Based on their theoretical discussion, the decay parameters might be functions of roughness and stability instead of constants. Panofsky and Mizuno (1975) continued the study and found that the relationship

30   between coherence and other parameters were rather complicated. A model for the decay parameter was proposed based on the discussion of its empirical properties. This model involves turbulence intensity accounting for the influence of terrain roughness, integral length scale which shows relationship with Richardson number, separation of the observations, and the angle between the wind direction and the measurement line. This model can be regarded as the first parameterization model for the Pielke and Panofsky's model, but it was just developed using very few observations measured with meteorological tower

35   and the dependence of coherence on separation and atmospheric stability was not adequately researched.

It is worth mentioning that wind evolution specifically refers to the longitudinal coherence (i.e. coherence in the direction of the flow) by definition. The longitudinal coherence differs from the lateral and vertical coherence because the former measures the correlation with respect to time lag while the latter with respect to spatial separation. However, in the above-mentioned studies the longitudinal coherence was not clearly distinguished. Kristensen (1979) proposed that the longitudinal coherence

40   should behave differently and deduced an alternative expression for wind evolution, which is known as Kristensen's model. This model is based on the assumption that the coherence can be modelled with the probability that an eddy measured at the first observation point will pass the second one.

In the recent years, wind evolution has become interesting again because of the new concept of lidar-assisted wind turbine control (see e.g. Schlipf, 2015; Simley and Pao, 2015; Simley et al., 2018). Lidar, more specifically, Doppler wind lidar is a

45   remote sensing device which can be used to measure wind speed in a certain spatial range (Weitkamp, 2005). The main idea of lidar-assisted wind turbine control is to enable a feedforward control of the wind turbine by using a nacelle-mounted lidar to measure the approaching wind field. The control system should only react to the changes in the wind field which can be predicted accurately over the distance to avoid harmful and unnecessary control action. This is made possible by applying an adaptive filter to filter the uncorrelated part of the lidar signal. An accurate prediction of the wind evolution will thus benefit the

50   filter design. Moreover, the application of Taylor's hypothesis in the wind field simulation is no longer appropriate for modelling the lidar-assisted control system. To solve this problem, Bossanyi (2013) proposed an approach to integrate the wind evolution model in the Veer's wind field simulation method (Veers et al., 1998) to make it possible to simulate a four-dimensional wind field.

Some attempts were made to improve the modelling of wind evolution. Schlipf et al. (2015) suggested an approach to

55   determine the decay parameter in the Pielke and Panofsky's model with measuring data of a nacelle-based lidar. Simley and Pao (2015) attempted to validate the Pielke and Panofsky's model and the Kristensen's model with data from LES wind fields and found out that the both models cannot always correctly model the coherence as frequency approaches zero. To improve this issue, Simley and Pao (2015) adapted the Pielke and Panofsky's model by introducing a new parameter to adjust the vertical intercept of the coherence model so that it can capture the decrease of the coherence at very low frequency. At the same time,

de Maré and Mann (2016) developed a four-dimensional model to describe the space-time structure of turbulence by combining the Mann spectral velocity tensor and the Kristensen's longitudinal coherence model.

Motivated by the above-mentioned research, this study aims to further analyze how wind evolution is influenced by the wind field conditions and to achieve a parameterization model for an empirical wind evolution model to predict the wind evolution according to relevant conditions, such as the wind statistics, atmospheric stability, and relative position of the measurement points. This is mainly done using lidar measurement because lidar can provide large amount of spatially separated measuring points simultaneously, which is a great advantage for studying the dependency of wind evolution on separation compared to meteorological tower. Some lidar data from two measurement campaigns undertaken in different terrain types are available. If any data of the meteorological tower is also available in the corresponding measurement campaigns, it is involved in the analysis to provide a comparison.

This study is carried out as follows: After the preliminary data processing, wind evolution is estimated with lidar data and fitted to a wind evolution model to obtain the model parameters. The distributions of the obtained wind evolution model parameters are analyzed to figure out some common characteristics. Then, the parameterization model is achieved by training a Gaussian Process Regression (GPR) model. The Automatic Relevance Determination Squared Exponential kernel (ARD-SE kernel) is applied to estimate the relative importance of the different wind field condition variables and to select the suitable input variables for the GPR model. Finally, the performance of the parameterization model is evaluated with a 5-fold cross-validation.

The present paper is organized as follows: Section 2 briefly explains the theoretical basis of wind evolution and the concept of the parameterization model as well as the principles of the applied methods in this work; Section 3 introduces the involved measurements and the procedure of the data processing; Section 4 presents the results of the statistical analysis of the wind evolution model parameters; Section 5 illustrates the process of the model training and the evaluation of the obtained parameterization models; Section 6 summarizes the presented results again and gives the conclusions and outlook of this study.

2 Methodology

This section first explains the mathematical definition of wind evolution in Sect. 2.1. Then, the model concept for the prediction of the wind evolution and the corresponding workflow of this study are presented in Sect. 2.2. After that, the wind evolution model applied in this work is introduced in Sect. 2.3. Finally, the details of the workflow are introduced and discussed in Sect. 2.3–2.7.

2.1 Wind Evolution

As mentioned in the introduction, wind evolution is mathematically defined as the magnitude-squared coherence between two wind speed signals i and j measured at two points separated in longitudinal direction, with i for the signal measured at upstream
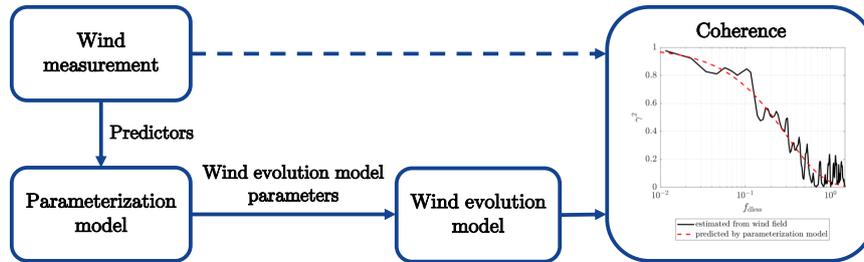
Figure 1. Concept of predicting the wind evolution by a parameterization model.

90 point and j for downstream point:

$$\gamma_{ij}^2(f) = \frac{|S_{ij}(f)|^2}{S_{ii}(f)S_{jj}(f)}, \tag{1}$$

where $S_{ii}(f)$ and $S_{jj}(f)$ represent the power-spectral densities (PSDs) of signals i and j, respectively, and $S_{ij}(f)$ represents the cross-spectral density between i and j. It must be emphasized that the coherence corresponds to a lagged correlation, which means the signal j should be shifted by the travel time Δt that the signal i is expected to arrive at the downstream point for

95 calculation of the coherence.

2.2 Concept and Workflow

It is aimed to predict the wind evolution, i.e. the coherence, but it is not possible to predict every point of the coherence curve. Therefore, a model is needed to describe the coherence with limited parameters, which then can be predicted by a parameterization model, i.e. a surrogate model. That is the wind evolution model. Figure 1 shows the prediction concept of this

100 work. The idea is first to predict the model parameters of the wind evolution model according to the wind field conditions by a parameterization model. Then, the coherence can be reconstructed with the wind evolution model using the predicted model parameters.

Based on this concept, the study is carried out as follows (see Fig. 2): 1) estimation of the coherence using lidar data; 2) determination of the wind evolution model parameters by fitting the estimated coherence to the wind evolution model; 3)

105 calculation of the potential predictors from the measured data; 4) training the Gaussian process regression model. More details are introduced in Sect. 2.3–2.7.

2.3 Wind Evolution Model

As explained above, it is very important to choose a wind evolution model that can match the trend of the coherence with only several simple parameters. A two-parameter wind evolution model, similar to the Simley's model (2015), is used in this study.
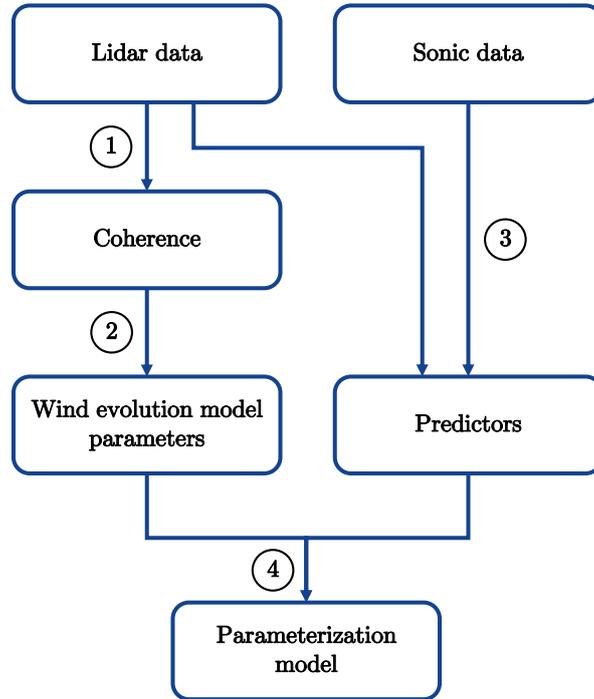
Figure 2. Workflow.

Following the theoretical considerations by Ropelewski et al. (1973), the coherence decreases exponentially with increasing travel time Δt of the signal with respect to "eddy turnover time" τ:

$$\gamma^2_{\mathrm{model}} = \exp\left(-C \cdot \frac{\Delta t}{\tau}\right), \tag{2}$$

where the term C represents the decay behaviour of the coherence depending on the time ratio. C is here virtual which can be a constant, a linear function, and even more complicated term.

τ is a time scale associated with the characteristic eddy size λ and characteristic velocity of turbulence which is approximated by the standard deviation of wind speed σ as following:

$$\tau \sim \frac{\lambda}{\sigma}. \tag{3}$$

This expression implies that eddies are supposed to decay faster under a high turbulence. Given the same degree of turbulence, large eddies are supposed to take longer time to decay.

The eddy size λ is linked to the frequency f and the flow mean wind speed U with this relation:

$$\lambda \sim \frac{U}{f}. \tag{4}$$
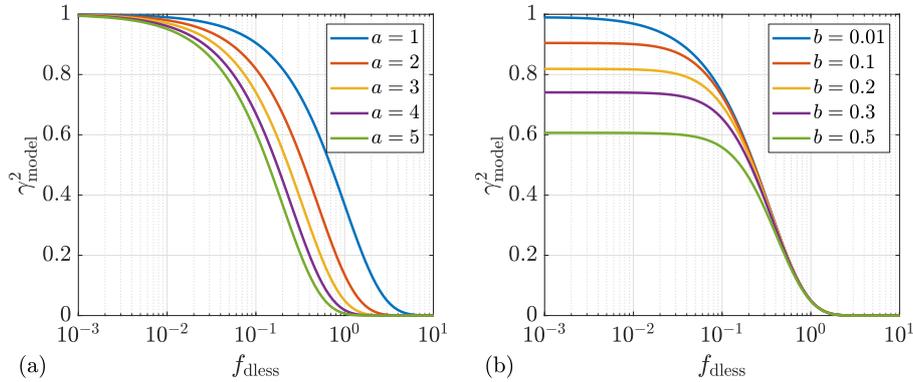
Figure 3. Impact of the model parameters a and b on the wind evolution model. (a) $b = 0$. (b) $a = 3$.

Combining Eq. (2)–(4) and introducing the second parameter in the model, as inspired by Simley's model (2015), the wind evolution model is finally defined as:

$$\gamma_{\mathrm{model}}^2 = \exp\left(-\sqrt{a^2 \cdot (f \cdot \Delta t)^2 + b^2}\right),\tag{5}$$

125   where the decay parameter a, which summarizes the term C and the other deduced terms, represents the decay effect of the coherence, and the offset parameter b is used to adjust the intercept (coherence for 0 frequency) of the modeled coherence curve. The intercept equals $\exp(-|b|)$. The both wind evolution model parameters are dimensionless. The benefit of introducing the offset parameter b is shown in Sect. 3.2. The travel time Δt is determined by the time lag of the peak of the cross-correlation between two signals, indicated as $\Delta t_{\mathrm{maxcorr}}$. In some previous studies, Δt is approximated by $\frac{d}{U}$ using Taylor's hypothesis (d

130   is separation), indicated as $\Delta t_{\mathrm{Taylor}}$. Considering the effect of induction zone of the wind turbine, this approximation is not applied in this study. The term $f \cdot \Delta t$ is dimensionless, and thus is defined as *dimensionless frequency* f_{dless}.

To give an overview of the wind evolution model, Fig. 3 shows the theoretical curves calculated with different values of a and b as example.

2.4   Estimation of Coherence using Lidar Data

135   In this work, the coherence is estimated with lidar data because lidar can provide more data sets with respect to different measuring separations for the estimation of the coherence, which is not easy to obtain from data of meteorological towers. And the prediction of the coherence is mainly expected to be applied coupled with the deployment of a lidar, e.g. in lidar-assisted wind turbine control.

A Doppler wind lidar is a remote sensing device measuring wind speed based on the optical Doppler effect. Lidar emits laser

140   pulses and detects the Doppler shift in backscattered light from the aerosol particles in the atmosphere that are entrained with the wind. The Doppler shift is proportional to the line-of-sight wind speed, i.e. the wind speed projected on the laser beam, and thus can be used to estimate the line-of-sight wind speed. The measurement principle of Doppler wind lidar is explained in many publications (see e.g. Weitkamp, 2005; Peña et al., 2013; Liu et al., 2019) and thus is not introduced here in detail.

However, it must be emphasized that the coherence estimated with lidar data is deviated from that estimated with data of point measurements, e.g. from two ultrasonic anemometers. There are several reasons for that: 1) The sampling rate of a lidar is generally much lower than that of an ultrasonic anemometer; 2) Lidar does not measure the wind speed at a point but the averaged wind speed over the measurement volume along the laser beam because of its measurement principle, which is the so-called spatial averaging effect of lidar; 3) Lidar can only measure the wind speed projected on its emitted laser beams, i.e. the light-of-sight wind speed. The influence of these three aspects is discussed as follows, specifically considering the case of starring mode of lidar:

Low sampling rate of lidar. According to the sampling theorem (oppenheim et al., 1997), the upper frequency limit of a signal transformed from the time domain into the frequency domain is the half of the sampling frequency. As long as the sampling rate of lidar is sufficiently high to acquire a complete coherence curve, it will not have a noticeable effect on the study of the coherence. To obtain as high sampling rate as possible, it is decided to select the data of the staring mode to calculate the coherence. The staring mode of lidar generally means the lidar measures the wind speed with a single laser beam pointing towards a fix direction. Specifically in this work, the laser beam points to the upstream of the wind turbine horizontally.

Spatial averaging effect of lidar. The spatial averaging effect can be modelled with a moving window averaging weighted by a Gaussian-like shape function centered at the measurement point.

Consider a pulsed lidar (only pulsed lidars are involved in this work), the weighting function $\mathrm{w}(x)$ is an even function centered at every measurement point along the laser beam. The lidar measured wind speed at the measurement point x_0 for any instant can be modelled with:

$$u_{\mathrm{l}}(x_0) = \int_{-\infty}^{\infty} \mathrm{w}(x_0 - x) u_{\mathrm{p}}(x) \mathrm{d}x = (\mathrm{w} * u_{\mathrm{p}})(x_0), \tag{6}$$

where $u_{\mathrm{p}}(x)$ is a function of the point measurement of the wind speed with respect to the x-axis aligned with the laser beam of the lidar.

According to the convolution theorem (oppenheim et al., 1997), the following relationship is valid for the Fourier transformation between space and wavenumber domain:

$$\mathcal{F}\{u_{\mathrm{l}}\} = \mathcal{F}\{\mathrm{w} * u_{\mathrm{p}}\} = \mathcal{F}\{\mathrm{w}\} \cdot \mathcal{F}\{u_{\mathrm{p}}\}, \tag{7}$$

where $\mathcal{F}\{\ \}$ is the Fourier transform operator.

Follow Eq. (1), the coherence estimated with lidar data, indicated with the subscript "l", is:

$$\gamma_{ij,\mathrm{l}}^2(f) = \frac{|S_{ij,\mathrm{l}}(f)|^2}{S_{ii,\mathrm{l}}(f) \cdot S_{jj,\mathrm{l}}(f)}, \tag{8}$$

where $S_{ii,\mathrm{l}}(f)$ and $S_{jj,\mathrm{l}}(f)$ are the auto-spectrum at the point i and j, respectively, $S_{ij,\mathrm{l}}(f)$ is the cross-spectrum between i and j, and f is the frequency in Hz. They are all estimated with lidar data. The auto-spectrum is:

$$S_{ii,\mathrm{l}}(f) = \mathcal{F}\{u_{i,\mathrm{l}}(t)\} \cdot \mathcal{F}^*\{u_{j,\mathrm{l}}(t)\}, \tag{9}$$

where $u_{i,l}(t)$ is the time series of the wind speed at i, and the symbol * means conjugate. And the cross-spectrum is:

$$S_{ij,l}(f) = \mathcal{F}\{u_{i,l}(t)\} \cdot \mathcal{F}^*\{u_{j,l}(t)\}. \tag{10}$$

Assume the laser beam is aligned with the wind direction and the Taylor's hypothesis is valid, Eq. (7) is also valid for the Fourier transformation between time and frequency domain by applying $t = \frac{x}{U}$, U is mean wind speed. Thus, Eq. (8) can be written as (t and f are omitted for clarity):

$$
\begin{aligned}
\gamma_{ij,l}^2 &= \frac{|\mathcal{F}\{u_{i,l}\} \cdot \mathcal{F}^*\{u_{j,l}\}|^2}{\mathcal{F}\{u_{i,l}\} \cdot \mathcal{F}^*\{u_{i,l}\} \cdot \mathcal{F}\{u_{j,l}\} \cdot \mathcal{F}^*\{u_{j,l}\}} \\
&= \frac{|\mathcal{F}\{w\} \cdot \mathcal{F}\{u_{i,p}\} \cdot \mathcal{F}^*\{w\} \cdot \mathcal{F}^*\{u_{j,p}\}|^2}{\mathcal{F}\{w\} \cdot \mathcal{F}\{u_{i,p}\} \cdot \mathcal{F}^*\{w\} \cdot \mathcal{F}^*\{u_{i,p}\} \cdot \mathcal{F}\{w\} \cdot \mathcal{F}\{u_{j,p}\} \cdot \mathcal{F}^*\{w\} \cdot \mathcal{F}^*\{u_{j,p}\}}.
\end{aligned} \tag{11}
$$

Because the function $w(x)$ is real and even, according to the conjugate symmetry of the Fourier transformation (oppenheim et al., 1997), $\mathcal{F}\{w\} = \mathcal{F}^*\{w\}$ and $\mathcal{F}\{w\}$ is real and even as well. As a result, all $\mathcal{F}\{w\}$ in the denominator and the numerator are cancelled out. And thus Eq. (11) becomes:

$$\gamma_{ij,l}^2 = \frac{|\mathcal{F}\{u_{i,p}\} \cdot \mathcal{F}^*\{u_{j,p}\}|^2}{\mathcal{F}\{u_{i,p}\} \cdot \mathcal{F}^*\{u_{i,p}\} \cdot \mathcal{F}\{u_{j,p}\} \cdot \mathcal{F}^*\{u_{j,p}\}} = \gamma_{ij,p}^2. \tag{12}$$

This means that the spatial averaging effect does not influence the coherence if the above-mentioned assumptions are fulfilled.

Misalignment of wind direction and lidar measurement. The above derivation is based on an important assumption that the laser beam is aligned with the wind direction. This will not always be fulfilled in the reality even for a nacelle based lidar conducting the starring mode.

Figure 4 shows a sketch for a case of misalignment of wind direction and lidar measurement. The coherence estimated with lidar data is γ_{12}^2. The coherence of the two longitudinal wind components at the point 1 and 2 and that of the corresponding line-of-sight wind speeds are the same when the both angles are the same, because the angles only introduce a same constant in the respective wind speed time series. However, γ_{12}^2 is no longer the pure longitudinal coherence only with respect to the longitudinal separation but the horizontal coherence (Panofsky and Mizuno, 1975), combined the effects of the longitudinal coherence γ_{23}^2 and the lateral coherence γ_{13}^2. To retrieve the longitudinal coherence in this case, the above discussed spatial averaging effect must be coupled to a specific turbulence model (Schlipf, 2015; Mann et al., 2009), and thus the wind evolution model is included in the final model implicitly.

In this study, it is decided to develop the parameterization model based on the horizontal coherence for the following reasons: First, a standalone parameterization model, independent from any turbulence model, is desired for more flexibility in application. Second, the determination of the model parameters of an implicit wind evolution model is complicated and it is a must to acquire the angle between the wind direction and the laser beam, which is not always possible in application, especially when considering lidar as the only data source. Since the prediction concept is expected to be applicable for different data availability. It is not desired to make the estimation of coherence depend on a variable which is not always guaranteed to be available. Third, consider the case for a nacelle based lidar, the presence of the misalignment of the lidar measurement means the wind turbine misalignment exists as well. In this case, it makes sense to predict the corresponding horizontal coherence.
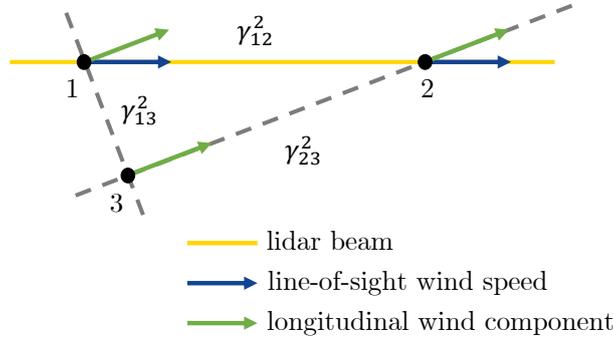
Figure 4. Sketch of misalignment of wind direction and lidar measurement.

Whereas, the variation in the horizontal coherence caused by the direction misalignment is attributed to the misalignment angle,
205 which is considered as one of the predictors (see Sect. 2.5).

Certainly, if the measurement of the direction misalignment is available in a given application scenario, the prediction concept can be easily adjusted by changing the model used in the second step in the workflow (see Sect. 2.2) to obtain the wind evolution model parameters.

2.5 Potential Predictors

210 Three groups of wind field condition variables are supposed to be relevant to wind evolution, and thus will be the potential predictors of the surrogate model. A discussion about these variables is presented as follows:

Wind statistics. As explained in Sect. 2.3, wind evolution is supposed to be correlated with the degree of turbulence or rather turbulent kinetic energy. Therefore, standard deviation σ, turbulence intensity I_T, integral length scale L, and integral time scale T are considered as representative variables. The integral time scale T is defined as (Pope, 2000):

215
$$T = \int_0^\infty \rho(s)\mathrm{d}s, \tag{13}$$

where $\rho(s)$ is the autocorrelation function. In this study the integral time scale is computed by integrating the autocorrelation up to the first zero crossing. Since it is not possible to calculate the integral length scale L based on its definition, it is approximated with the integral time scale T:

$$L = U \cdot T. \tag{14}$$

220 Moreover, it is interesting to study the influence of other statistical characteristics on wind evolution, such as the third standardized central moment skewness $\tilde{\mu}_3$, a measure of the asymmetry of the distribution of the wind speeds in a data block, and the fourth standardized central moment kurtosis $\tilde{\mu}_4$, a measure of the "tailedness".

Atmospheric stability. The atmospheric stability represents a global effect of the boundary layer on the wind field, and thus it is considered as an influence factor on the wind evolution. The atmospheric stability is usually characterized with Monin-

Obukhov length or Richardson number. In this study a dimensionless height ζ built with Monin-Obukhov length L_{MO} is used as stability indicator. Because it is found a functional relationship between the dimensionless height ζ and the gradient Richardson number for flat terrain (Businger et al., 1971), these two variables are supposed to be equivalent for representing the influence of stability in the surrogate model. The dimensionless height ζ is defined as (Businger et al., 1971):

$$\zeta = \frac{z}{L_{\mathrm{MO}}} = -\frac{\kappa g \overline{w'\theta'_{\mathrm{v}}} z}{\overline{\theta} u_*^3},\tag{15}$$

where κ is von Kármán constant, g is gravitational acceleration, z is the measurement height, $\overline{\theta}$ is average of potential temperature, u_* is friction velocity, and $\overline{w'\theta'_{\mathrm{v}}}$ is covariance of perturbations of vertical velocity and virtual potential temperature.

Relative position of the measurement points. The distance between the two measurement points d is likely to play an important role in the wind evolution because it determines how far the eddies travel, and thus how likely or to what extent the local terrain changes. So as the travel time Δt. For prediction, it is not possible to obtain $\Delta t_{\mathrm{maxcorr}}$. Therefore, the travel time approximated using Taylor's Hypothesis $\Delta t_{\mathrm{Taylor}}$ is considered as predictor.

As discussed in Sect. 2.4, the angle between the lidar beam and the main wind direction α is associated to the influence of the lateral coherence on the horizontal coherence, and thus is considered as a relevant variable. And it is important to analyze to what extent the horizontal coherence would depend on this angle.

It is emphasized that the variables discussed above are "potential" predictors of the parameterization model according to physical consideration. Further analysis needs to be done to determine which of them should be selected for model training, which is called *feature selection*. The principle of feature selection is to figure out variables which provide best predictive power (accounting to most of the variation of the model responses) and ideally, these variables should be independent from each other to prevent over-fitting in model training. Since one of the objectives is to figure out the necessary predictors under different data availability, different combinations of predictors are discussed in Sect. 5.

The Table 1 lists the notations of the potential predictors used in this work. These variables are acquired from data of lidar and/or ultrasonic anemometers according to the data availability of the measurement campaign. This is distinguished with subscripts: "l" for lidar and "s" for ultrasonic anemometer. For example, U_{l} means mean wind speed calculated with lidar data while U_{s} means that calculated with data from ultrasonic anemometer (hereinafter for brevity, also referred to as sonic data).

2.6 Gaussian Process Regression

In the preliminary study it is found out that the Gaussian Process Regression (GPR) overall performs the best for the prediction of the wind evolution model parameters (Chen, 2019). Therefore, in the present work, attempt is made to further analyze the applicability of the GPR model for this purpose taking into account different measurement scenarios. This section briefly introduces the principle of the Gaussian process regression (GPR) and the most important model hyperparameters which modify the behaviour of a GPR model. The model training is done using Matlab Statistics and Machine Learning Toolbox.

The principle of GPR. Think of making a regression model from some data. A very intuitional approach is fitting the data to certain types of function, e.g. linear function or polynominal function. However, this requires an initial guess about the underlying functions of the data, which is very difficult in this case, because the wind evolution model parameters do not

Table 1. Notations of potential predictors.

U	mean wind speed $[\mathrm{m\,s^{-1}}]$
σ	standard deviation of wind speed $[\mathrm{m\,s^{-1}}]$
$\tilde{\mu}_3$	skewness of wind speed [-]
$\tilde{\mu}_4$	kurtosis of wind speed [-]
I_T	turbulence intensity [-]
T	integral time scale [s]
L	integral length scale [m]
ζ	dimensionless Obukhov length [-]
d	distance [m]
α	angle between lidar beam and main wind direction [°]

indicate any clear dependency on the potential predictors. The reasons could be multiple: first, the data could be noisy; second, the dependency could exist in multidimensional space which is not possible to be observed in a single dimension, etc. Under this circumstance, GPR turns out to be a good choice because it is non-parametric probabilistic model, which means the model is not a "fix" function but a probability distribution over functions. The principle of the GPR is based on the Bayesian inference. The prior distribution over functions, which can be understood as a guess about what kind of functions could be present without knowing the data, is specified by a particular Gaussian process (GP) which favours smooth functions. In the training process, as adding the data, the distribution over functions is adjusted in the way that the probability of the functions which do not agree with the observations will be decreased, which gives the posterior distribution over the functions (Rasmussen and Williams, 2006).

Hyperparameters of GPR. The behaviour of a GPR model is defined by its hyperparameters. To introduce the hyperparamters, a basic explanation in mathematical aspect is given following Rasmussen and Williams (2006).

The GPR is based on the Bayesian inference. The Bayesian linear regression model with Gaussian noise is defined as:

$$f(\boldsymbol{x}) = \phi(\boldsymbol{x})^\top \boldsymbol{w}, \quad y = f(\boldsymbol{x}) + \varepsilon, \tag{16}$$

where $\boldsymbol{x}$ is the input vector of different parameters, $\phi(\boldsymbol{x})$ is the function which maps the input vector into a higher dimensional space where the Bayesian linear model is applicable, $\boldsymbol{w}$ is the weight vector of the linear model, $f(\boldsymbol{x})$ is the function value, y is the observed value, and ε is independent identically distributed Gaussian noise with zero mean and variance σ_n^2:

$$\varepsilon \sim \mathcal{N}(0, \sigma_\mathrm{n}^2). \tag{17}$$

275 The Bayesian linear model is a GP given the prior of $\boldsymbol{w}$ is Gaussian distributed with zero mean. Since a GP is fully specified by its mean and covariance, it is written as:

$$f(\mathbf{X}) \sim \mathcal{GP}(\mathbf{0}, \mathrm{cov}(f(\mathbf{X}))), \tag{18}$$

where $\mathbf{X}$ is the aggregation of all input vectors. This is the prior distribution over functions. The presence of ε shows another advantage of the GPR that it is able to inherently assume noisy observations and take into account this effect in the model. σ_{n}

280 is one of the hyperparameters.

It is common but not necessary to assume GPs with zero mean function. The use of basis functions makes it possible to specify a non-zero mean over functions. So, the model can also be assumed as:

$$g(\boldsymbol{x}) = f(\boldsymbol{x}) + \mathbf{h}(\boldsymbol{x})^\top \boldsymbol{\beta}, \tag{19}$$

where $\mathbf{h}(\boldsymbol{x})$ are a set of basis functions and $\boldsymbol{\beta}$ are the corresponding coefficients. Basis function is one of the hyperparameters.

285 The coefficients $\boldsymbol{\beta}$ are estimated with training data.

The covariance of the function values is usually acquired through a kernel function:

$$\mathrm{cov}(f(\mathbf{X})) = \mathrm{K}(\mathbf{X}, \mathbf{X}). \tag{20}$$

There are two types of kernel functions: one is kernel functions with same characteristic length scale for each predictor; the other is that with separate characteristic length scale. The latter is called Automatic Relevance Determination kernel functions

290 which can be used to select predictors. Kernel function and its characteristic length scale are hyperparameters of GPR model.

In this work, the Automatic Relevance Determination Squared Exponential kernel function (ARD-SE kernel) is applied. ARD-SE kernel function is basically the squared exponential kernel function with a separate characteristic length scale σ_{m} for each predictor m (m is the index of predictors). For any pairs of observations i, j, the ARD-SE kernel function is defined as:

$$\mathrm{K}(\boldsymbol{x_i}, \boldsymbol{x_j}) = \sigma_f^2 \exp\left[-\frac{1}{2} \sum_{m=1}^{D} \frac{(x_{im} - x_{jm})^2}{\sigma_m^2} \right], \tag{21}$$

295 where σ_f^2 denotes the signal variance, which determines variation of function values from their mean. The length scale σ_m implies the sensitivity of the function being modeled to the predictor m. A relatively large length scale indicates a relatively small variation along the corresponding dimensions in the function, which means these predictors are less relevant in comparison to the others (Duvenaud, 2014).

In the end, the key predictive equation for GPR can be derived by conditioning the joint Gaussian prior distribution on the

300 observations:

$$\boldsymbol{f_*} | \mathbf{X}, \boldsymbol{y}, \mathbf{X}_* \sim \mathcal{N}(\overline{\boldsymbol{f}}_*, \mathrm{cov}(\boldsymbol{f_*})), \tag{22}$$

where the subscription * denotes test data. $\boldsymbol{f_*}$ represents $\boldsymbol{f}(\boldsymbol{X_*})$ for convenience.

To summarize, the hyperparameters defining the GPR model are the basis function $\mathbf{h}(\boldsymbol{x})$, the noise standard deviation of the Gaussian process model σ_{n}, the kernel function $\mathrm{K}(\boldsymbol{x_i}, \boldsymbol{x_j})$, the standard deviation of the function values σ_{f}, and the length

305 scale in the kernel function σ_{m}. These hyperparameters can be tunned in the training process to achieve a better model.

2.7 Model Validation

The trained model is evaluated with a k-fold cross-validation, in which the data is divided into k disjoint, equally sized subsets. The model validation is done with one subset (also called in-fold observations) and the training is done with the rest k-1 subsets (also called out-of-fold observations). This procedure is repeated k times, each time with a different subset for validation. The

310   predicted target values and the goodness-of-fit measures of the regression models are computed for in-fold observations using a model trained on out-of-fold observations. In this study, 5-fold cross-validation was applied.

The model performance is evaluated with two goodness-of-fit measures: the Root Mean Square Error (RMSE) and the coefficient of determination (R^2), which are defined with Eq. (23) and Eq. (24), respectively.

$$\text{RMSE} = \sqrt{\frac{1}{N}\sum_i^N (y_i - y_{pred,i})^2}, \tag{23}$$

315

$$R^2 = 1 - \frac{\sum_i^N (y_i - y_{pred,i})^2}{\sum_i (y_i - \overline{y})^2}, \tag{24}$$

In Eq. (23) and Eq. (24) y and y_{pred} denote the observed target values and the predicted one, $\overline{y}$ denotes the average of the observed target values, N denotes the number of observations.

It is worth mentioning that according to this definition R^2 can be understood as taking prediction with mean value of the

320   observations as reference to evaluate the model performance. In this case R^2 ranges from $-\infty$ to one, for perfect prediction. R^2 yields zero if the prediction is simply made with the mean value of the observations. The higher the R^2 is, the better the model performs. A negative R^2 indicates that the prediction with the selected model is even worse than the prediction just using the mean value of the observations.

3   Data Processing

325   This section first introduces the data sources in Sect. 3.1 and then explains the procedure for the determination of the wind evolution model parameters in Sect. 3.2.

3.1   Data Source

In this study, measured data from two research projects are involved. The reasons for using two different data sources are on the one hand to find commonality in two different measurements and avoid accidental conclusions, and on the other hand, to

330   study whether there are differences or what kind of differences in the wind evolution can be observed. The relevant research projects as well as the measurement campaigns are briefly introduced as follows:

LidarComplex. The research project LidarComplex was funded by the German Federal Ministry for Economic Affairs and Energy (BMWi). In this project, a lidar measurement campaign was carried out in Grevesmühlen, Germany. The measurement site is basically flat, mainly farmland with hedges and few large trees. The SWE Scanner 1.0, which has five measurement

335 range gates (can be understood as measurement distances), was installed on a wind turbine with a roter diameter of $109\,\mathrm{m}$ in the measurement campaign. A meteorological mast is located $295\,\mathrm{m}$ southwest of the wind turbine on which the lidar was installed. The SCADA data of the wind turbine is also available. More details about the measurement campaign can be found in Schlipf et al. (2015).

The data of the ultrasonic anemometer installed on 93 m height is used in this study. Instead of the meteorological coordinate
340 system, the wind coordinate system with x-axis aligning to the main wind direction is more useful for the analysis of wind evolution. Thus, the longitudinal (indicated with the subscript "x") and the lateral (indicated with the subscript "y") wind speeds are obtained by projecting the high-resolution time series wind speed on this coordinate system. The main wind direction is determined with the mean wind direction for each data block.

ParkCast. The research project ParkCast[1] is an ongoing project funded by the German Federal Ministry for Economic
345 Affairs and Energy (BMWi). Currently, a lidar measurement campaign is being conducted on the offshore wind farm alpha ventus. Two long-range lidars StreamlineXR have been deployed in the measurement campaign. The data used in this study was gathered by the one installed on the nacelle of the wind turbine AV4 measuring the inflow stream. Unfortunately, the data of the FINO1 and the SCADA data of the AV4 for the observed period was not yet available when the analysis was done. Therefore, it has to be assumed that the wind turbine had no direction misalignment during the observed period and the lidar
350 was always measuring along the main wind direction.

In comparison to ultrasonic anemometers, lidar systems have much lower sampling rate because of its measurement principle. To obtain as high sampling rate as possible, it is decided to select the measurement periods where the staring mode was conducted for the both campaigns.

Essential information about the measurements are summarized in the Table 2. Figure A1 gives an overview of the wind
355 statistics of these two selected measurement periods by illustrating the relative frequency distribution of lidar measured wind speed and lidar measured turbulence intensity. For brevity, "LidarComplex" and "ParkCast" are used to refer the selected measurements throughout the paper.

3.2 Determination of Wind Evolution Model Parameters

To obtain the wind evolution model parameters a and b, the wind evolution is estimated with lidar data and then fitted to the
360 wind evolution model (Eq. 5). The processing procedure is described as follows:

Step 1: Filtering of the lidar data.

The lidar data from LidarComplex is filtered using a CNR filter with the valid range from -24 dB to -5 dB.

The lidar data from ParkCast is filtered with a range filter which is originally applied in image processing but adapted for lidar data filtering for the long-range lidar by Würth et al. (2018). In comparison to the CNR filter, the range filter removes
365 less valid data points while ensuring the filter quality. Its approach is to detect the extreme values which exceed the threshold within certain number of adjacent data points defined by the window size. A range filter is applied to check the line-of-sight

---

[1]https://www.rave-offshore.de/en/parkcast.html

Table 2. Summary of measurement setups.

	LidarComplex	ParkCast
Selected period	02 Dec 2013 - 20 Dec 2013	04 June 2019 - 14 June 2019
Location	Grevesmühlen, Germany	Alpha Ventus
Terrain type	onshore, flat	offshore
Device	nacelle based lidar + met mast	nacelle based lidar
Measurement height [m]	95 (lidar), 93 (sonic)	92
Range gate [m]	54.5:27.25:163.5	30:60:990
Number of range gates	5	17
Sampling rate [Hz]	0.99	0.27
Valid samples*	3285	10112

*After lidar data filtering, data pairing, and outlier filtering. Details see 3.2

wind speed of lidar and its standard deviation. The thresholds for both are 6 m/s and 3 m/s, respectively. The window size is set as three data points.

Step 2: Estimation of coherence.

370   The lidar data is divided into 30-min blocks. This is also consistent with the common used period for calculation of the Obukhov length. Only the data blocks with more than 80% valid data points are used to estimate the coherence. The missing values are interpolated with the shape-preserving piecewise cubic interpolation. And the missing end values are replaced with their nearest value.

The data measured at different range gates (i.e. measurement distance) is paired in the way shown in Fig. 5 to obtain as many
375   samples (i.e. data blocks) as possible. The pairing has C_N^2 possibilities (N is the number of the lidar range gates).

The travel time of the wind field is approximated with the time lag at the maximum of the cross-correlation $\Delta t_{\mathrm{maxcorr}}$ between these two wind speed signals. The upstream point is always regarded as reference point. The data measured at the downstream is shifted by $\Delta t_{\mathrm{maxcorr}}$.

The magnitude-squared coherence is estimated using Welch's overlapped averaged periodogram method using Hamming
380   window, 24 segments, and 50% overlap.

The data of the reference point is used to calculate the lidar measured wind statistics.

Step 3: Fitting to the wind evolution model.

Because both lidars are installed on the top of the wind turbine nacelle and the nacelle is actually moving with certain frequencies, the focus points of lidar are thus moving as well. This movement causes excitation at certain frequencies in the
385   estimated coherence.
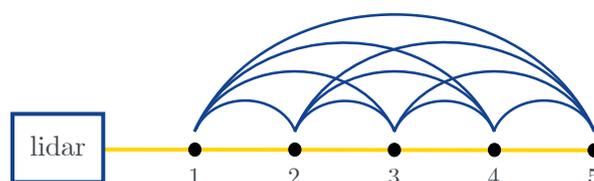
Figure 5. Pairing of different measurement points for estimation of coherence. LidarComplex as example.

Figure A2 shows a comparison between an example coherence curve and the power spectral density (PSD) of the fore-aft and in-plane tower top acceleration of LidarComplex. The excitation in the coherence conforms to that in the both PSDs and is mainly located in the frequency range higher than $0.2\,\mathrm{Hz}$. To avoid the negative effect on the fitting quality caused by this excitation, the cut-off frequency is set to be $0.2\,\mathrm{Hz}$ and the coherence is only fitted up to this cut-off frequency.

390   The fitting is done through nonlinear least squares fitting using Levenberg-Marquardt algorithm. Only the data blocks with R^2 of the fitting higher than 0.8 are considered as valid samples.

Step 4: Outliers filtering.

The final filtering was done by checking the value distribution of every parameter to omit outliers. It is emphasized that outlier is not necessarily wrong data. For some cases, outlier is just sample collected from the value range where not enough

395   samples have been collected. Though, it is very important to filter the outliers properly because it is difficult for the regression model to capture the relationship for those value ranges with few samples. The outliers are determined as the data with value higher than the 99th percentile of the data.

Figure 6 is an example plot of the data block 07 Dec. 2013 12:00-12:30 from LidarComplex. This data block is selected as a representative case study example for LidarComplex and is referred througout the paper. The figure illustrates the estimated

400   coherence between different range gates and the corresponding fitted curves. The shaded areas show the cut-off frequency of $0.2\,\mathrm{Hz}$ is reasonable for this case. A similar plot from ParkCast is found in Fig. A3. Because the sampling rate of ParkCast is lower, the excitation by the nacelle top movement is not observed in the coherence, and thus no cut-off frequency was set for ParkCast data.

In Fig. 6 (c) and (d) the intercept of the coherence is much lower than one even though the separation is not very large.

405   This confirms the necessity of choosing a wind evolution model which is able to define different offset values depending on the conditions. Indeed, in comparison to the fitting quality of Pielke and Panofsky's model which merely contains a single parameter — the decay parameter a, the fitting quality of the wind evolution model (Eq. (5)) is overall better (see Fig. A4). The R^2 of the fitting to Eq. (5) is almost always higher than that of the fitting to the Pielke and Panofsky's model. The wind evolution model used in this work (Eq. (5)) is thus proven to be able to model the coherence better.
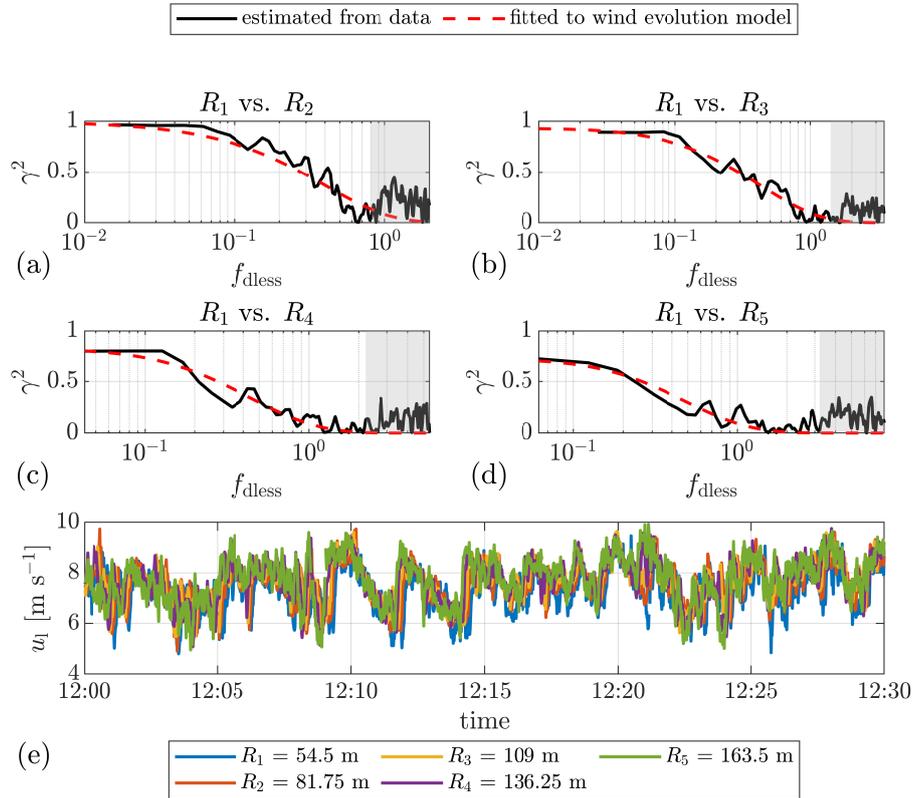
Figure 6. (a) – (d) Example plots of the estimated coherence between the lidar wind speeds measured at different range gates and the corresponding fitted curves. The separations between the corresponding range gates are $27.25\,\mathrm{m}$, $54.5\,\mathrm{m}$, $81.75\,\mathrm{m}$, and $109\,\mathrm{m}$, respectively. The shaded areas indicate the data filtered by the cut-off frequency $0.2\,\mathrm{Hz}$. (e) Time series of the lidar wind speed. The mean lidar wind speed $U_1 = 7.3\,\mathrm{m\,s^{-1}}$. Date: 07 Dec. 2013. Data source: LidarComplex.

4 Statistical Analysis of Wind Evolution

This section presents the results of the statistical analysis of the wind evolution, including the distributions of the wind evolution model parameters, in Sect. 4.1 and their dependency on the measuring separation in Sect. 4.2.

4.1 Distribution of the Wind Evolution Model Parameters

To study the overall characteristics of the wind evolution, the value distributions of the wind evolution model parameters for the both measurements are displayed in Fig. 7.

As listed in Table 2, there are two main differences between the lidar settings in the both measurements: sampling rate and measurement range, which might affect the distributions of the wind evolution parameters. To enhance the comparability of the both distributions, two special post-processings are executed correspondingly. Firstly, because the lidar sampling rate of

LidarComplex is approximately as three times as that of ParkCast, an artificial data set is made for LidarComplex by averaging
420   every three data points of the original lidar data to simulate the lidar data as if it were measured with a similar sampling rate as
that of ParkCast, so that the distributions of the both measurements can be compared. The fitted probability density function
(PDF) of the wind evolution model parameters determined with this data set are plotted as yellow dashed lines in Fig. 7 (a) and
(b). The comparison between the fitted PDF of the original data and that of the data with reduced sampling rate indicates that the
lidar sampling rate only very slightly affects the wind evolution model parameters, or perhaps more accurately, the estimated
425   coherence. Hence, the different sampling rates of the both measurements do not account for the differences between the both
cases observed in Fig. 7. Secondly, because of the limited measurement range of LidarComplex the maximum separation
between two range gates only reaches $109\,\mathrm{m}$, while that of ParkCast reaches more than $700\,\mathrm{m}$. To make them comparable, Fig.
7 (c) and (d) merely show the wind evolution parameters calculated from the coherence with separation smaller than $120\,\mathrm{m}$ of
ParkCast.

430   Apart from that, the measurements were carried out in different environments (onshore and offshore), at different times of
the year (which would impact atmospheric stability), and have different wind speed and turbulence intensity distributions (see
Fig. A1). Despite these differences, the value distributions of the wind evolution model parameters do have some common
characteristics. First of all, the value ranges of the both wind evolution model parameters for the both measurements are
similar, a ranges mostly from 0 to 6 and b from 0 to 0.5. Values out of these ranges are less likely to happen according to the
435   measurements. Second, the values of a and b are found out to follow an inverse Gaussian distribution and a Gamma distribution,
respectively. These two PDFs are determined by fitting the histograms to all the PDFs supported by MATLAB and searching
for the one with the maximum likelihood.

The corresponding fitted parameters of the PDFs (orange curves) are displayed in Table 3. It is interesting to observe that
the peak of the probability density is located around $a = 1.8$ for the onshore case LidarComplex, while around $a = 0.8$ for the
440   offshore case ParkCast. Moreover, the medians of a are approx. 2.0 and 1.5 for LidarComplex and ParkCast, respectively. The
mean (see μ in Table 3) and median of a as well as its value of the peak location of the PDF of LidarComplex are all higher than
that of ParkCast. This indicates that the coherence under similar separation generally decays faster in an onshore location than
an offshore location. In terms of b, most of the values is near 0 and values higher than 0.1 are not often observed. Therefore,
the y-axes in Fig. 7 (b) and (d) are shown in logarithmic manner to make the part of higher value of b visible. However, there
445   is no significant difference of b between both cases observed in the figure.

It is not yet possible to explain the physical relationship between the wind evolution model parameters and the above-
mentioned PDFs and the physical meaning of the corresponding PDF parameters. To verify whether the above discussed
phenomena commonly exist in wind evolution, further research involving more different measurement campaigns is necessary.
At this point, a hypothesis is made that the values of a and b might follow an inverse Gaussian distribution and a Gamma
450   distribution, respectively. The corresponding PDF parameters probably depend on the terrain types on the one hand. It is
not clear if the roughness length would be the suitable parameter to quantify the influence of the terrain type on the value
distribution of wind evolution model parameters. To figure out a concrete relationship between the PDF parameters and the
terrain types, again, it is necessary to involve more measured data gathered from different terrain types. On the other hand,

Table 3. Parameters of the fitted probability density functions.

wind evolution model parameters	PDF	LidarComplex	ParkCast
a	inverse Gaussian distribution $\mathrm{f}(x;\mu,\lambda) = \sqrt{\frac{\lambda}{2\pi x^3}}\exp\left[-\frac{\lambda(x-\mu)^2}{2\mu^2 x}\right]$	$\mu = 2.07$ $\lambda = 17.23$	$\mu = 1.86$ $\lambda = 2.38$
b	Gamma distribution $\mathrm{f}(x;k,\theta) = \frac{1}{\Gamma(k)\theta^k}x^{k-1}e^{-\frac{x}{\theta}}$	$k = 0.42$ $\theta = 0.18$	$k = 0.24$ $\theta = 0.16$

The notations μ, λ, k, θ are independent from the other notations out of the table.
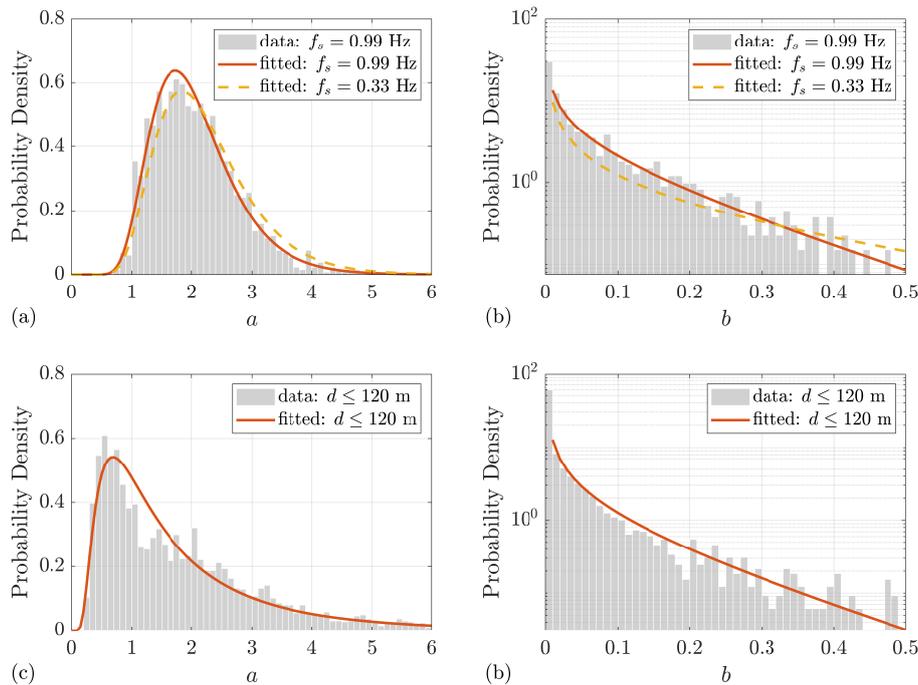
Figure 7. Distribution of wind evolution model parameters. (a) and (b): LidarComplex. (c) and (d): ParkCast. The curves show the corresponding fitted probability density function.

unfortunately, it is not yet possible to estimate to what extent the atmospheric stability would affect the distribution of the wind evolution model parameters because there was no sonic data available for ParkCast to do the relevant research until this work was finished.

4.2 Dependency of the Wind Evolution Model Parameters on Measuring Separation

Figure 8 shows the fitted curves of the estimated coherence of all pairings of the above-mentioned case study example of LidarComplex. The same color indicates the pairings have a common range gate, while the same marker indicates the pairings
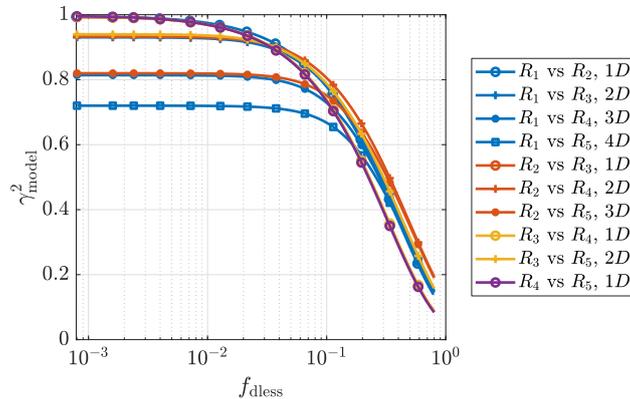
Figure 8. Fitted curves of the estimated coherence between the lidar wind speeds measured at different range gates. The range gate R_1 to R_5 locate at $54.5\,\mathrm{m}$, $81.75\,\mathrm{m}$, $109\,\mathrm{m}$, $136.25\,\mathrm{m}$, and $163.5\,\mathrm{m}$, respectively. $1D = 27.25\,\mathrm{m}$. The mean lidar wind speed $U_l = 7.3\,\mathrm{m\,s^{-1}}$. Date and time: 12 Dec. 2013 12:00-12:30. Data source: LidarComplex.

460 have the same measuring separation. From the figure it can be observed a very clear dependency of the fitted curve form on the measuring separation – The curves with the same marker are overlapped despite different range gates. This confirms that the coherence only depends on the relative position but has nothing to do with the absolute position, even though the measurement points are located in the induction zone of a wind turbine, which is defined as the range of 2.5 rotor diameters in the inflow side of the wind turbine. Since the curve offset is only related to the offset parameter b, obviously, b must strongly depends on

465 the measuring separation. In addition, that all the fitted curves of the coherence are grouped together proves it is reasonable to model the wind evolution based on the dimensionless frequency. Similar conclusions can be drawn from the example plot of ParkCast (see Fig. A5), which proves these conclusions are not accidental.

To further study the dependency of the wind evolution model parameters on the measuring separation, the box plots of the wind evolution parameters grouped by the measuring separations are given in Fig. 9. Although the ranges of the measuring

470 separation of the both measurements are very different, similar trends can still be observed from the box plots. The decay parameter a shows a decreasing trend with increasing measuring separation. This decreasing trend of a gradually stops when the separation approaches $300\,\mathrm{m}$ as observed in Fig. 9 (c). The offset parameter b shows an increasing trend with increasing measuring separation. An increasing b implies a decrease of the offset of the coherence curve. This is consistent with the phenomena observed from Fig. 8 and Fig. A5.

475 The decay of the coherence is supposed to result from the evolution of the turbulence eddies with respect to the travel time. The dependency of the decay parameter a on the measuring separation, or rather the travel distances, actually reveals the dependency of a on the travel time. Figure 10 shows the correlation between a and the travel time approximated by $\Delta t_{\mathrm{maxcorr}}$ of ParkCast. The fitted curve represents a negative correlation trend between them. This implies that the decay rate of the coherence decreases with an increasing travel time. The fitting is done through nonlinear least squares fitting with Levenberg-

480 Marquardt algorithm.
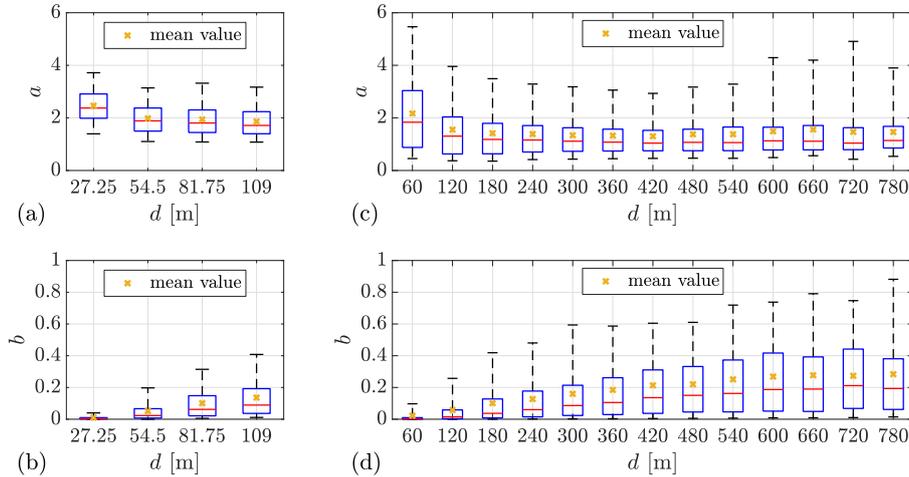
Figure 9. Box plots of the wind evolution model parameters grouped by the measuring separations d. The bottom and top of the boxs indicate the first (25th percentile) and the third (75th percentile) quartile. The lower and upper whiskers show 5th (bottom) and 95th (top) percentiles. The red line in the middle indicates the median value. Minimum sample size is 50.
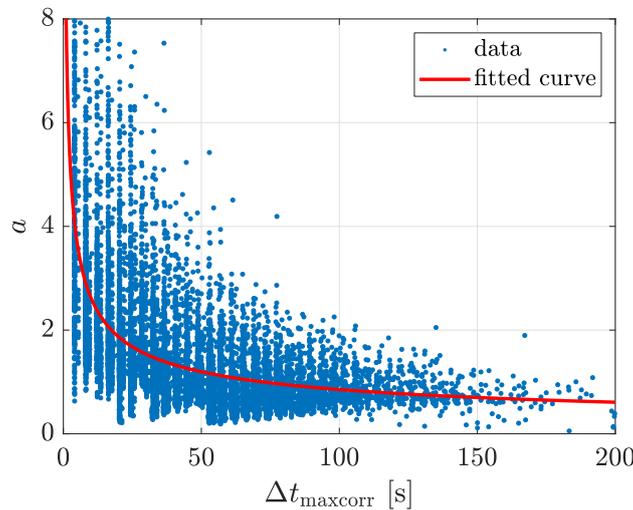
Figure 10. Correlation between the decay parameter a and the travel time approximated by $\Delta t_{\text{maxcorr}}$. The equation of the fitted curve: $a = 8.06 \cdot \Delta t_{\text{maxcorr}}^{-0.49}$. Data source: ParkCast.

5 Parameterization Model

This section first presents the training procedure of the GPR model with application of the ARD-SE kernel to select the suitable predictors in Sect. 5.1. Followed is a discussion about the predictor selection in Sect. 5.2 and an evaluation of the model performance of the GPR models for the prediction of the wind evolution model parameters in Sect. 5.3.
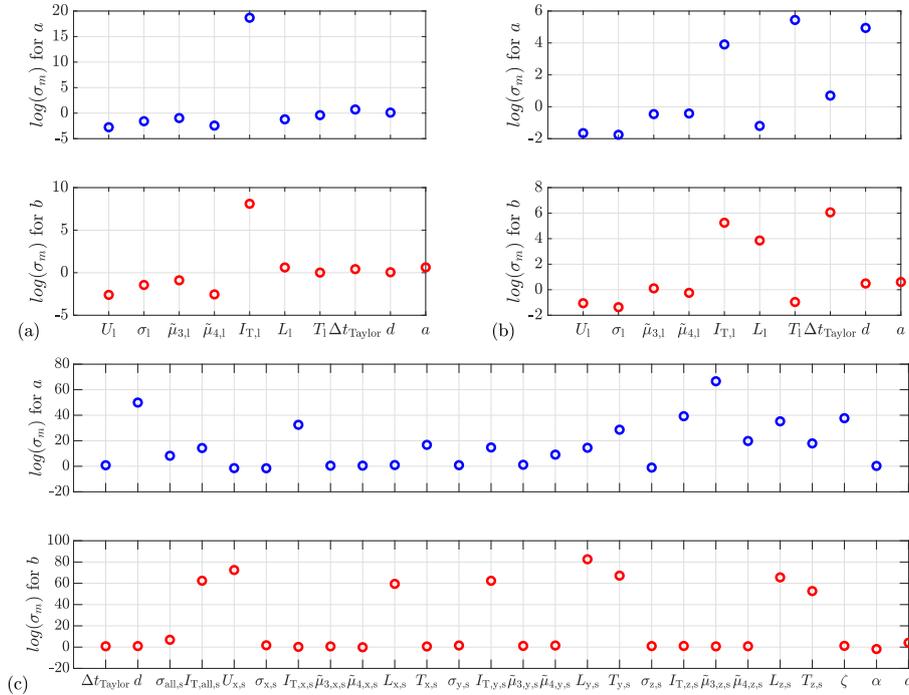
Figure 11. Comparison of the relative importance of the predictors. (a) ParkCast, lidar data. (b) LidarComplex, lidar data. (c) LidarComplex, sonic data.

5.1 Model Training

485

The model training is a two-step process. In the first step, all the potential predictors are included in a preliminary model training to determine the characteristic length scale σ_m for each predictor (see Eq. 21). As explained in Sect. 2.6, a relatively large $\log(\sigma_m)$ indicates that the corresponding predictor is less relevant to the model, and thus is not a suitable or necessary predictor for the model, and vice versa. Figure 11 illustrates a comparison among the $\log(\sigma_m)$. In the second step, the predictors

490 are selected according to different preset limits of the $\log(\sigma_m)$ considering different cases of application or data availability, e.g. if only lidar data is available or if sonic data is also available. The models are trained again using the corresponding selected predictors with application of a 5-fold cross validation. The corresponding RMSE (see Eq. 23) and R^2 (see Eq. 24) are calculated and used as criteria for the evaluation and comparison of the model performance.

The initial settings of the GPR model training is listed in Table 4. The setting of "exact GPR" means a standard GPR is

495 applied in the fitting and prediction process. In contrast, the GPR can be approximated using different methods to reduce the computational time for large amount of training data. The initial values of σ_n, σ_f, and σ_m listed in the table are used to initiate the training. The final values are determined by the training data. The standardization is done by centering and scaling the data of each predictor by its mean and standard deviation, respectively, which gives the standard scores (also called z-scores) of the predictor data. When the standardization is activated, the training is done using the standardized predictor data.

Table 4. Initial settings of GPR model training.

Basis function	constant
Kernel function	ARD-SE
Fitting method	exact GPR
Prediction method	exact GPR
Initial value of σ_n	standard deviation of observed responses
Initial value of σ_f	standard deviation of observed responses
Initial value of σ_m	10
Standardization	true

5.2 Discussion of Predictor Selection

In the predictor selection, two different situations of data availability are considered: only using variables calculated with lidar data as predictors (in both of LidarComplex and ParkCast available) and only using variables calculated with sonic data (only in LidarComplex available). The main focus of this study is to evaluate the possibility to predict the wind evolution only using lidar data. Including the situation of only using sonic data aims to provide a comparison.

Table 5 shows the different predictor combinations and the corresponding limit values of the $\log(\sigma_m)$ for the both wind evolution model parameters and for the both measurements. The corresponding R^2 and RMSE of the 5-fold cross validation are also listed in the table. The bold text indicates the recommended predictor combinations for each situation. The recommendation principle is achieving as high model performance as possible with as few predictors as possible.

The overall performance of the GPR model is satisfactory — in all situations, the R^2 of the recommended cases are over 0.65 and for the best case can even reach 0.8 (see case 14). These results are much better than that of the preliminary study (Chen, 2019), especially the prediction accuracy of the offset parameter b has been significantly improved. This is attributed to the application of the ARD-SE kernel in this study, whereas in the preliminary study, kernel functions with a common length scale for predictors were tried. Moreover, for the cases of using lidar data, the same predictors are selected for the both measurements despite the very different measurement conditions, which proves the corresponding predictor combinations are not accidental. Therefore, it is believed that the ARD-SE kernel is able to select reasonable predictors for the GPR model. As shown in Table 5, the predictors with $\log(\sigma_m)$ lower than 1.0 are generally essential for the model. The limit of $\log(\sigma_m)$ can be set to 0 if the number of predictors needs to be reduced while the model performance should be kept acceptable.

The following points about predictor selection are worth discussing:

Selection between two related variables. In the preliminary training, two pairs of related variables are intentionally involved at the same time: standard deviation σ and turbulence intensity I_T, integral time scale T and integral length scale L. Only

Table 5. Results of model cross validation.

Measurement	Target	Case	$log(\sigma_m)$	Predictors	RMSE	R^2
ParkCast lidar data	a	1	< 1.0	$U_1, \sigma_1, \tilde{\mu}_{3,1}, \tilde{\mu}_{4,1}, L_1, T_1, \Delta t_{\text{Taylor}}, d$	0.66	0.70
		2	< 0	$U_1, \sigma_1, \tilde{\mu}_{3,1}, \tilde{\mu}_{4,1}, T_1, \Delta t_{\text{Taylor}}$	**0.65**	**0.71**
ParkCast lidar data	b	3	< 1.0	$U_1, \sigma_1, \tilde{\mu}_{3,1}, \tilde{\mu}_{4,1}, L_1, T_1, \Delta t_{\text{Taylor}}, d, a$	0.11	0.67
		4	< 0.1	$U_1, \sigma_1, \tilde{\mu}_{3,1}, \tilde{\mu}_{4,1}, T_1, d$	**0.11**	**0.66**
		5	< -0.8	$U_1, \sigma_1, \tilde{\mu}_{3,1}, \tilde{\mu}_{4,1}$	0.16	0.32
LidarComplex lidar data	a	**6**	< 1.0	$U_1, \sigma_1, \tilde{\mu}_{3,1}, \tilde{\mu}_{4,1}, L_1, \Delta t_{Taylor}$	**0.41**	**0.67**
		7*	-	$U_1, \sigma_1, L_1, \Delta t_{\text{Taylor}}$	0.46	0.58
		8	< -1.0	U_1, σ_1, L_1	0.50	0.52
LidarComplex lidar data	b	9	< 1.0	$U_1, \sigma_1, \tilde{\mu}_{3,1}, \tilde{\mu}_{4,1}, T_1, d, a$	0.044	0.74
		10	< 1.0	$U_1, \sigma_1, \tilde{\mu}_{3,1}, \tilde{\mu}_{4,1}, T_1, d$	**0.048**	**0.69**
LidarComplex sonic data	a	11	< 2.0	$U_{\text{x,s}}, \sigma_{\text{x,s}}, \tilde{\mu}_{3,\text{x,s}}, \tilde{\mu}_{4,\text{x,s}}, L_{\text{x,s}}, \Delta t_{\text{Taylor}}, \sigma_{\text{y,s}}, \tilde{\mu}_{3,\text{y,s}}, \sigma_{\text{z,s}}, \alpha$	0.33	0.79
		12	< 0.5	$U_{\text{x,s}}, \sigma_{\text{x,s}}, \tilde{\mu}_{3,\text{x,s}}, \tilde{\mu}_{4,\text{x,s}}, \sigma_{\text{z,s}}, \alpha$	0.40	0.69
		13	< 0	$U_{\text{x,s}}, \sigma_{\text{x,s}}, \sigma_{\text{z,s}}$	**0.40**	**0.69**
LidarComplex sonic data	b	**14**	< 1.0	$\tilde{\mu}_{3,\text{x,s}}, \tilde{\mu}_{4,\text{x,s}}, L_{\text{x,s}}, \Delta t_{\text{Taylor}}, \sigma_{\text{y,s}}, I_{\text{T,z,s}}, \tilde{\mu}_{4,\text{z,s}}, L_{\text{z,s}}, a$	**0.039**	**0.80**
		15	< 0.5	$\tilde{\mu}_{3,\text{x,s}}, L_{\text{x,s}}, a$	0.080	0.14

* Case 7 is selected to compare with case 6 to see the effect of $\tilde{\mu}_3$ and $\tilde{\mu}_4$ on the model.

one of the two related variables needs to be selected as predictor if necessary, because they can be converted to each other. In terms of σ and I_{T}, it is surprising to notice that the GPR model shows a preference for σ rather than I_{T}, although I_{T} is more commonly used in data analysis and simulation in wind energy. However, the situation becomes complicated in terms of T and L. The GPR model shows a slight preference for T in most of the cases of using lidar data except in the case 6–8 where L is
525 clearly more preferred. Considering that L is actually approximated by the multiplication of T and the mean wind speed (see Eq. (14)) and the relationship between σ and I_{T} is also similar, it is possible that the GPR model generally tends to select the variable calculated from the data but not from the other variables.

Introducing higher-order wind statistics as predictors. In literature, the higher-order statistics skewness and kurtosis of the wind speed are not considered in the study of the wind evolution. However, it is interesting to observe that they are selected as
530 predictors for all the cases of using lidar data besides the mean and the standard deviation. The comparison between the case 6 and 7 proves that introducing skewness and kurtosis as predictors can indeed improve the prediction accuracy of the wind evolution. This also implies that the skewness and the kurtosis probably contain additional information which can describe the state of turbulence more concretely. For example, given the same mean wind speed and standard deviation, a positive or a negative skew could indicate two different states of the turbulence, which could further be associated with other conditions.
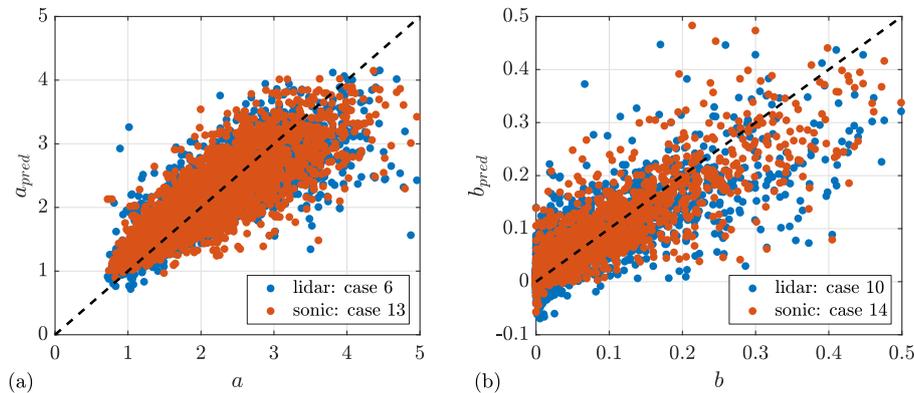
Figure 12. Comparison of prediction performance of models using lidar data and sonic data of LidarComplex. The subscript "pred" indicates the predicted values.

535   *Introducing one of the targets as a predictor for the other.* Since the two wind evolution parameters jointly determine the shape of the wind evolution model, there is a certain correlation between them. Introducing one of them as a predictor for the other may improve its prediction accuracy. The comparison of case 9 and 10 confirms that introducing a as a predictor for b can indeed increase the R^2 of the prediction of b. This means it could be a good idea to predict the wind evolution model parameters successively rather than separately. This concept is not yet fully studied in this work, and thus case 9 is not

540 considered as recommendation. To prove its applicability it is necessary to investigate which wind evolution model parameter should be first predicted and how the prediction uncertainty of the first one would be propagated to the second one.

   Prediction using sonic data. As mentioned above, the research on the cases of using sonic data as predictors is involved to provide a comparison. Figure 12 illustrates a comparison between the model performance of the recommended cases of using lidar data and sonic data. It must be emphasized that the ultrasonic anemometer is installed on a met mast located at $295\,\mathrm{m}$

545 away from the lidar. There must be a deviation between the sonic data and the data of the wind field where the coherence is estimated. Despite this, the best cases of using sonic data as predictors (case 11 and 14) show a higher prediction accuracy, R^2 of about 0.8, in comparison to that of using lidar data (case 6 and 9). This implies that the upper limit of the prediction accuracy will be higher if sonic data is used. Moreover, case 13 shows a slightly better result than that of case 6, with only three predictors: the mean and standard deviation of the longitudinal component $U_{\mathrm{x,s}}$ and $\sigma_{\mathrm{x,s}}$, and the standard deviation of

550 the vertical component $\sigma_{\mathrm{z,s}}$. Think of the physical consideration of Kristensen (1979). The Kristensen's model assumes that the wind evolution is determined by two probabilities: one is the probability that the eddy decays within the travel time; the other is the probability that the eddy diffuses in the transversal direction. The former could be associated with $U_{\mathrm{x,s}}$ and $\sigma_{\mathrm{x,s}}$, while the latter with $\sigma_{\mathrm{z,s}}$. This could be an explanation for this predictor combination.

WIND
ENERGY
SCIENCE
DISCUSSIONS

eawe
european academy of wind energy
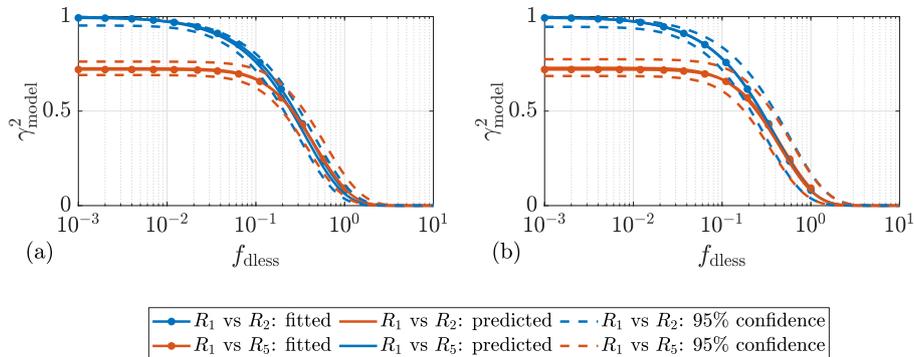
Figure 13. Example predicted coherence with 95% confidence interval for two different measuring separations of LidarComplex. (a) Prediction with lidar data: predicted value of a from case 6 and that of b from case 10. (b) Prediction with sonic data: predicted value of a from case 13 and that of b from case 14. The input predictor data and the estimated coherence are from the case study example of LidarComplex: 12 Dec. 2013 12:00-12:30.

5.3 Model Evaluation

555 As mentioned above, the prediction accuracy of the parameterization model using lidar data as predictors is satisfactory, showing an R^2 at least over 0.65. Section 5.2 already covers some contents of model evaluation, from the perspective of the prediction of the wind evolution model parameters. In this section, model evaluation is further discussed from other perspectives.

Firstly, it is interesting to visualize the predicted coherence in the frequency domain, combining the prediction of the both
560 wind evolution model parameters. Figure 13 shows the predicted coherence and the corresponding 95% confidence interval by the GPR models using lidar data (case 6 and 10) and sonic data (case 13 and 14) for the case study example of LidarComplex, respectively. The predicted coherence and the 95% confidence interval are reconstructed through putting the predicted value of a and b and their lower and upper bounds of the 95% confidence interval into the wind evolution model (Eq. (5)). From the figure, it can be observed that the prediction is very good because the predicted coherence is almost overlapped with the one
565 estimated from the measured data and the 95% confidence interval is quite narrow.

Secondly, it is important to check if the prediction errors of the models are relevant to the values of the predictors. Taking the models trained with the lidar data of LidarComplex (case 6 and 10) as example, Fig. 14 and 15 illustrate the box plots of the prediction errors, defined as the deviation between the predicted target value and the real one, with respect to the values of the predictors. The histograms of the predictor values are plotted below the box plots correspondingly. The x-axes of the
570 box plots correspond the upper limit of the respective bin in the histograms. For example, in Fig. 14 (a), the first box labelled with "4" means it is plotted with the prediction errors of the samples attributed to the mean wind speed range of 3–4 ms^{-1}. To avoid accidental conclusions, there is a minimum requirement of the sample size of 50 for the box plots. The distributions of the prediction error of a and b are all centered around 0 and no obvious relevance between the error and values of any of
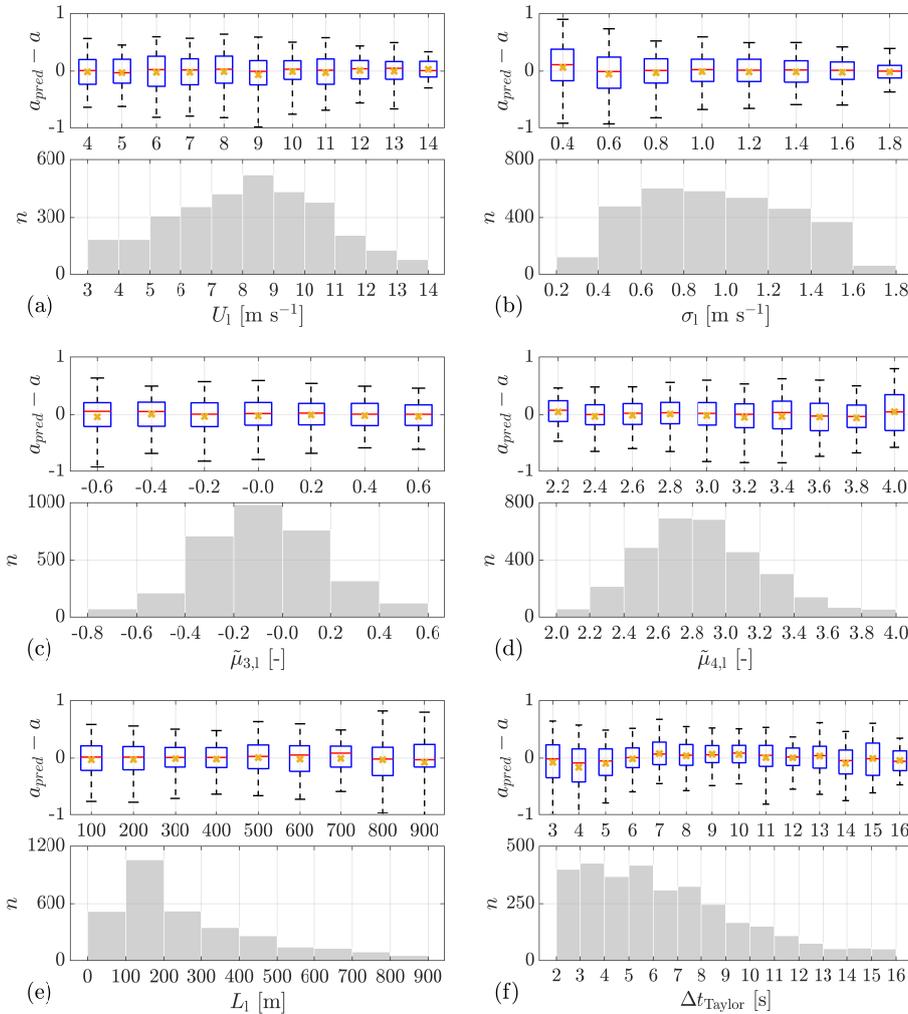
Figure 14. Prediction error of a of case 6 with respect to the values of the predictors. n is sample size. The bottom and top of the boxs indicate the first and the third quartile, i.e. 25th and 75th percentile, respectively. The lower and upper whiskers show 5th and 95th percentiles. The red line and the yellow cross in the middle indicate the median and mean value, respectively.

the predictors is indicated in the both figures. For some cases, the range of the whiskers is relatively large because of a small
575 sample size.

    As a result, it is proven that the Gaussian process regression is capable of achieving an accurate parameterization model for the wind evolution. However, it is worth emphasizing that the performance of any regression model is only possible to be as good as the quality of the training data. No matter what kind of regression model cannot eliminate the noisy term in the training data. And the noisy the training data is, the more uncertainty the prediction of the regression model will contain. A good data
580 source is always very essential for training a good regression model.
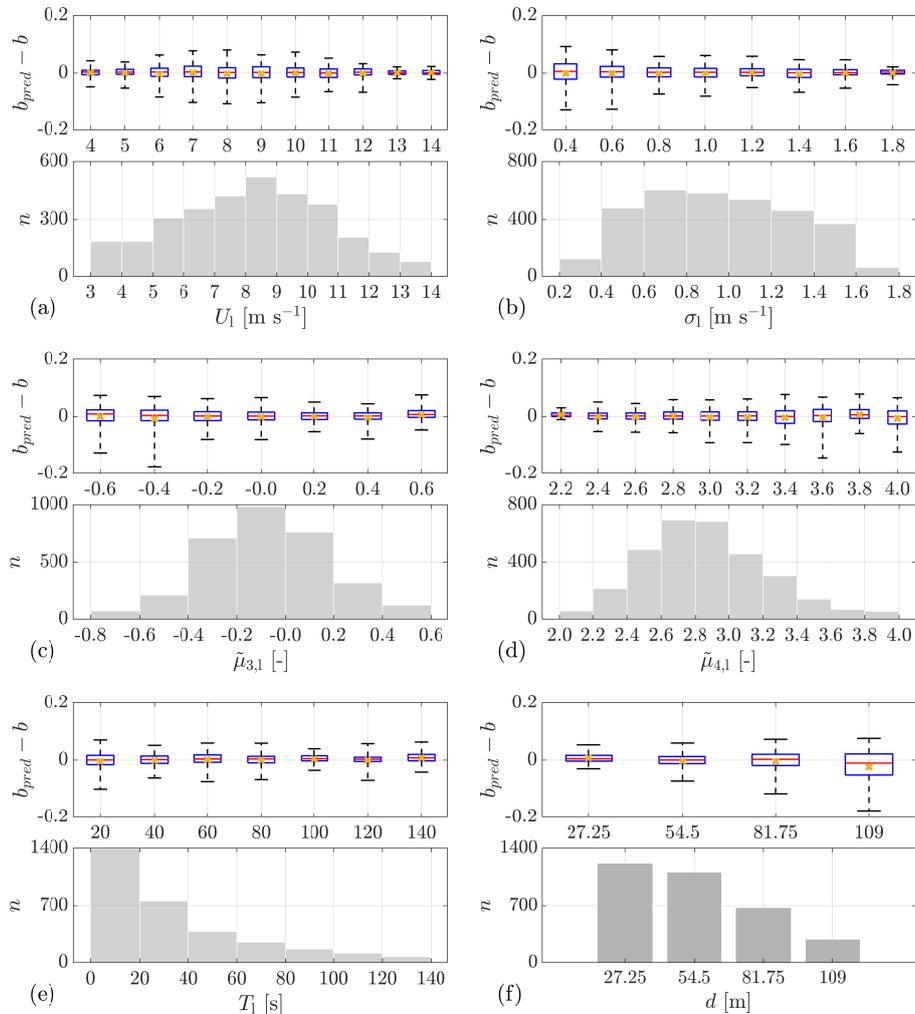
Figure 15. Prediction error of b of case 10 with respect to the values of the predictors. n is sample size. The bottom and top of the boxs indicate the first and the third quartile, i.e. 25th and 75th percentile, respectively. The lower and upper whiskers show 5th and 95th percentiles. The red line and the yellow cross in the middle indicate the median and mean value, respectively.

6 Conclusions and Outlook

This paper aims to achieve a parameterization model for the wind evolution model to predict the wind evolution according to the wind field conditions. Because the concept of the lidar-assisted wind turbine control needs the aid of an accurate model for the prediction of the wind evolution to avoid harmful and unnecessary control action.

585   For this purpose, a two-parameter wind evolution model suggested in literature was applied to model the wind evolution. Some data of two nacelled based lidars and an ultrasonic anemometer of two measurements carried out in an onshore and an offshore location were involved in the study. The wind evolution, i.e. the coherence between two measuring points, was

estimated using the lidar data and the wind evolution model parameters a and b were determined by fitting the estimated coherence to the wind evolution model. The relevant wind field condition variables were derived from the data of the lidars and

590   the ultrasonic anemometer.

Two main outcomes are presented: a statistical analysis of the wind evolution model parameters to reveal some characteristics of them and an investigation of the applicability of the Gaussian process regression for prediction of the wind evolution model parameters.

In the statistical analysis, the distributions of the wind evolution model parameters of the both measurements show some

595   common characteristics, despite different wind field conditions and settings of the measurements. The value ranges of the both wind evolution parameters a and b are very similar in the both measurements. The distributions of a and b seem to follow an inverse Gaussian distribution and a Gamma distribution, respectively. The fitted parameters of the probability density functions are different in the both measurements. It is thus hypothesized that the parameters of the probability density functions should depend on the terrain type. But it was not possible to analyze the influence of the atmospheric stability due to the lack

600   of necessary data. Moreover, it was observed a strong dependency of wind evolution model parameters on the measuring separation. The decay parameter a shows a decreasing trend with increasing measuring separation, while the offset parameter b shows an increasing trend with increasing measuring separation.

The applicability of Gaussian process regression to achieve the parameterization model was investigated. The trained models show satisfactory prediction accuracy under a 5-fold cross validation. The automatic relevance determination squared expo-

605   nential kernel was applied to evaluate the relative importance of the predictors for the model and select the essential predictors. It is confirmed that this kernel is capable of selecting the reasonable predictors under different data availability cases. Some interesting insights are given by the predictor selection, e.g. introducing higher-order wind statistics or one of the predicted targets as predictors can improve the prediction accuracy of the model. The model performance is also evaluated by a visualization of the predicted coherence and its 95% confidence interval in the frequency domain. The predicted coherence matches

610   the coherence estimated with the measured data very well and the 95% confidence interval is relatively narrow. In addition, it was analyzed whether the prediction errors is relevant to the values of the predictors. No obvious relevance can be observed. As a result, it is proven that the Gaussian process regression is capable of achieving a parameterization model with sufficient accuracy for the prediction of the wind evolution.

For the model performance of the parameterization model, there is still space for improvement. Since the performance of

615   any regression model is only possible to be as good as the quality of the training data, reducing the uncertainty in the training data or increasing the data amount could improve the model performance. For example, methods to improve the estimation of the coherence and the wind statistics from lidar data are desired. Moreover, the predictors discussed above do not cover all the possibilities. Introducing new proper predictors could also improve the model performance. In fact, the model concept is very flexible. Any improvement of any part of the workflow can be easily integrated.

620   In the future, besides the ideas above-mentioned, it is interesting to involve more measurement data, especially from different terrain types, to further study if the characteristics of the wind evolution found out in this work commonly exist and what are the physical principles behind them. Another question needs to be answered is if it is possible to achieve a generally
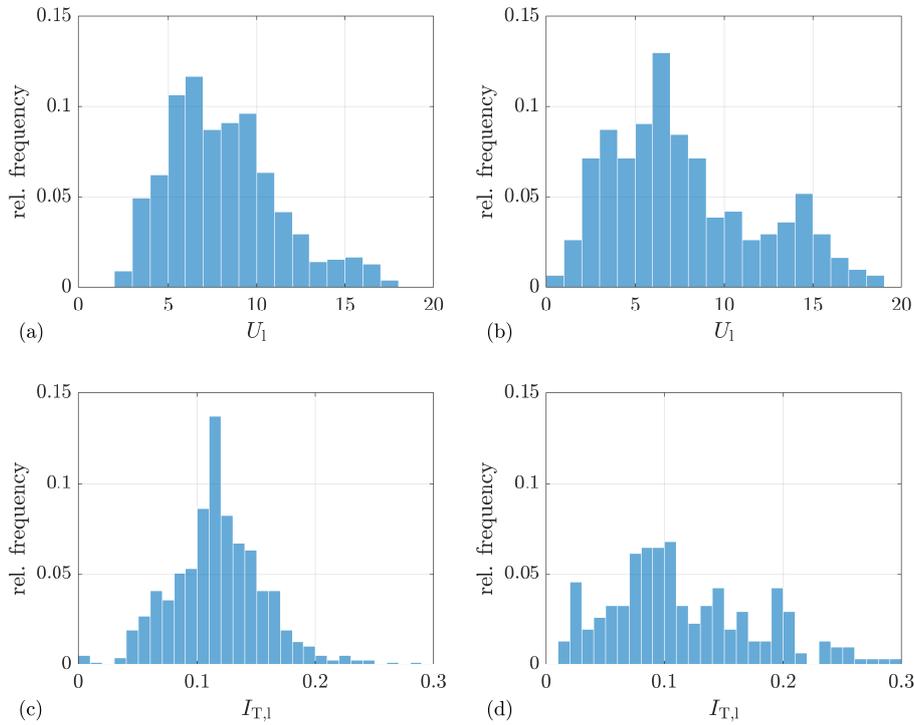
Figure A1. Distribution of lidar measured mean wind speed and turbulence intensity for the selected period. (a) and (c) are from LidarComplex, measurement point at $163.5\,\mathrm{m}$; (b) and (d) are from ParkCast, measurement point at $150\,\mathrm{m}$.

applicable parameterization model and how. Moreover, considering that the computational time of the model training could be an important issue for some applications, e.g. real-time model training, it is worth doing a comparison between the Gaussian
625   process regression and some alternative algorithms to provide an insight of the trade-off between the computational time and the prediction accuracy of the model. Furthermore, consider the application of the parameterization model using real-time measurement data as predictors, an additional model will be needed to determine whether the current data meets the quality requirements to be input into the parameterization model. This will be one of the research focuses in the near future.

Last but not least, as mentioned above, the model concept is very flexible and the methodology can be applied in different
630   situations. For example, for other lidar trajectories or even other measurement devices, the model concept can be modified by replacing the method of the estimation of coherence. The wind evolution model and the regression model can also be changed. Basically, one can achieve a parameterization model to meet own specific requirements following the concept and the methodology presented in this paper.
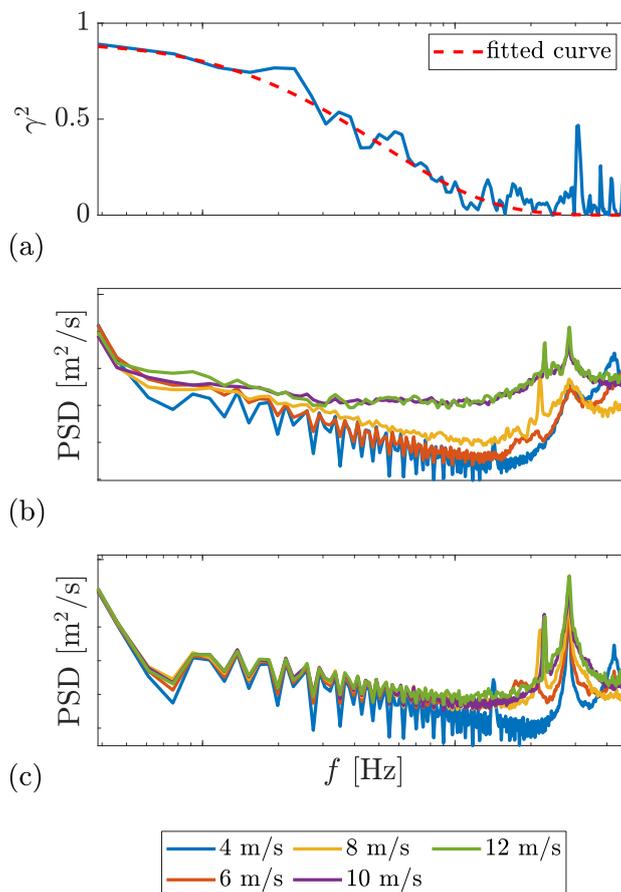
Figure A2. (a) Example coherence: $U_1 = 11.7\,\mathrm{m\,s}^{-1}$, $d = 81.75\,\mathrm{m}$, $R^2 = 0.95$. (b) and (c) are PSDs of the fore-aft and in-plane tower top acceleration, respectively. The x-axis is logarithmic. Date and time: 07 Dec. 2013 12:00 - 12:30. Data Source: LidarComplex. Because of data protection it is not allowed to show any values concerning the turbine properties.

Author contributions. YC conceived the concept, developed the model codes, processed the data, created the figures, conducted the analysis,
and prepared the manuscript. DS and PWC provided general guidance and essential suggestions throughout the process. PWC supervised
the research.

Competing interests. The authors declare that they have no conflict of interest.

Acknowledgements. This research is carried out within the framework of Joint Graduate Research Training Group Windy Cities supported
by Ministry of Baden-Wuerttemberg for Sciences, Research and Arts. Some data used in this work is generated in the project LidarComplex

635
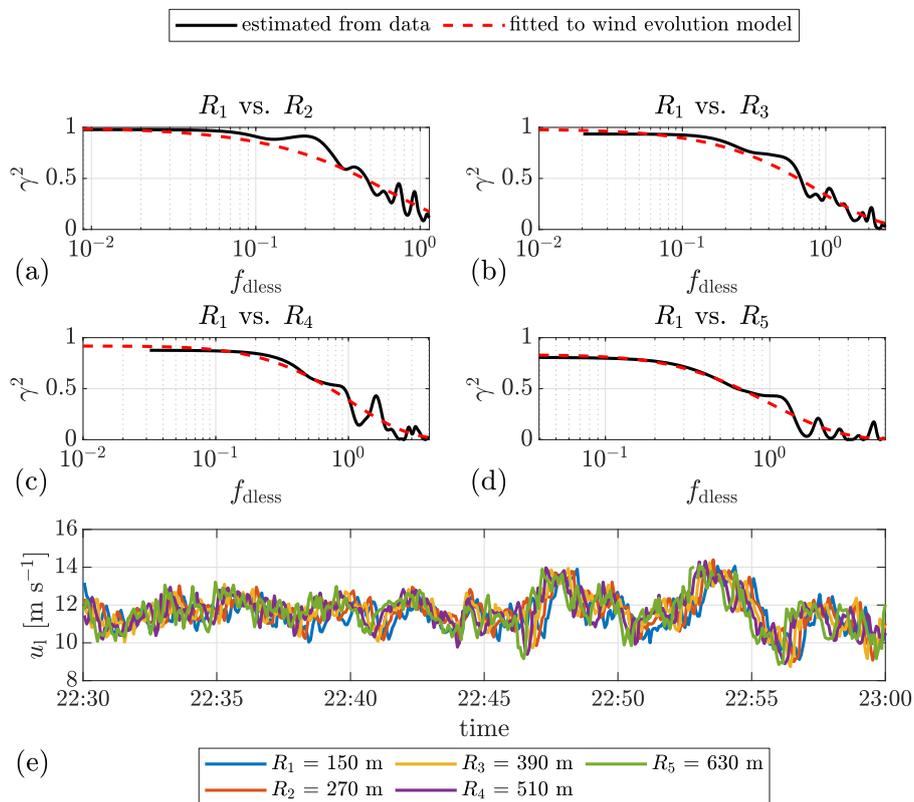
Figure A3. (a) – (d) Example plots of the estimated coherence between the selected range gates R and the corresponding fitted curves. The corresponding measurement distances are $120\,\text{m}$, $240\,\text{m}$, $360\,\text{m}$, and $480\,\text{m}$, respectively. (e) Time series of the lidar wind speed. The mean lidar wind speed is $11.6\,\text{m\,s}^{-1}$. Date: 12 June 2019. Data source: ParkCast.

640 (code number: 0325519A) and ParkCast (code number: 0324330A) which are funded by the German Federal Ministry for Economic Affairs and Energy (BMWi). This publication is supported by the Open Access Publications funding of University of Stuttgart.
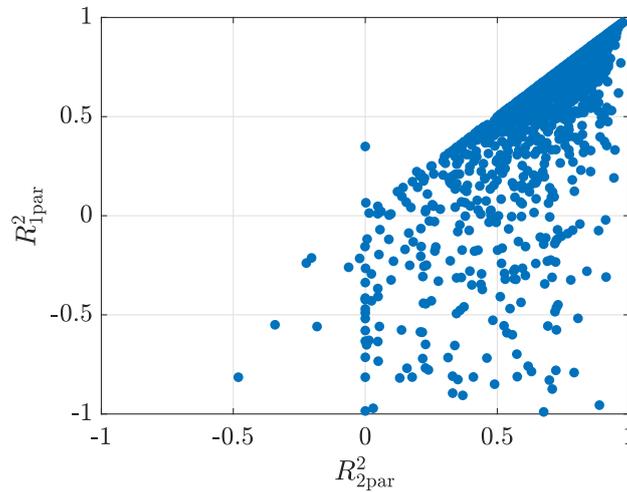
Figure A4. Comparison of R^2 of the fitting to the two-parameter wind evolution model (subscription "2par") and that of the fitting to the one-parameter one (subscription "1par").
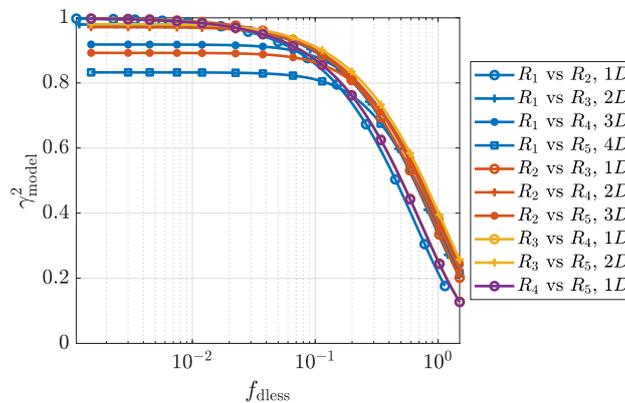
Figure A5. Fitted curves of the estimated coherence between the lidar wind speeds measured at different range gates. The range gate R_1 to R_5 are located at $150\,\mathrm{m}$, $270\,\mathrm{m}$, $390\,\mathrm{m}$, $510\,\mathrm{m}$, and $630\,\mathrm{m}$, respectively. $1D = 120\,\mathrm{m}$. The mean lidar wind speed $U_l = 11.6\,\mathrm{m\,s^{-1}}$. Date and time: 12 June 2019 22:30-23:00. Data source: ParkCast.

References

Bossanyi, E.: Un-freezing the turbulence: Application to LiDAR-assisted wind turbine control, IET Renewable Power Generation, 7, 321–329, https://doi.org/10.1049/iet-rpg.2012.0260, 2013.

645 Businger, J. A., Wyngaard, J. C., Izumi, Y., and Bradley, E. F.: Flux-Profile Relationships in the Atmospheric Surface Layer, Journal of the Atmospheric Sciences, 28, 181–189, https://doi.org/10.1175/1520-0469(1971)028<0181:FPRITA>2.0.CO;2, 1971.

Chen, Y.: Parameterization of wind evolution model using lidar measurement, https://doi.org/10.5281/zenodo.3366119, 2019.

Davenport, A. G.: The spectrum of horizontal gustiness near the ground in high winds, Quarterly Journal of the Royal Meteorological Society, 87, 194–211, https://doi.org/10.1002/qj.49708737208, 1961.

650 de Maré, M. and Mann, J.: On the Space-Time Structure of Sheared Turbulence, Boundary-Layer Meteorology, 160, 453–474, https://doi.org/10.1007/s10546-016-0143-z, 2016.

Duvenaud, D.: Automatic model construction with Gaussian processes, Apollo - university of cambridge repository, https://doi.org/10.17863/CAM.14087, 2014.

Kristensen, L.: On longitudinal spectral coherence, Boundary-Layer Meteorology, 16, 145–153, https://doi.org/10.1007/BF02350508, 1979.

655 Liu, Z., Barlow, J. F., Chan, P.-W., Fung, J. C. H., Li, Y., Ren, C., Mak, H. W. L., and Ng, E.: A Review of Progress and Applications of Pulsed Doppler Wind LiDARs, Remote Sensing, 11, 2522, https://doi.org/10.3390/rs11212522, 2019.

Mann, J., Cariou, J.-P. C., Parmentier, R. M., Wagner, R., Lindelöw, P., Sjöholm, M., and Enevoldsen, K.: Comparison of 3D turbulence measurements using three staring wind lidars and a sonic anemometer, Meteorologische Zeitschrift, 18, 135–140, https://doi.org/10.1127/0941-2948/2009/0370, 2009.

660 oppenheim, A. V., Willsky, A. S., and Nawab, S. H.: Signals & systems, Prentice-Hall signal processing series, Prentice Hall and London : Prentice-Hall International, Upper Saddle River, 2nd ed. edn., 1997.

Panofsky, H. A. and Mizuno, T.: Horizontal coherence and Pasquill's beta, Boundary-Layer Meteorology, 9, 247–256, https://doi.org/10.1007/BF00230769, 1975.

Peña, A., Hasager, C., Lange, J., Anger, J., Badger, M., Bingöl, F., Bischoff, O., Cariou, J.-P., Dunne, F., Emeis, S., Harris, M., Hofsäss, M.,
665 Karagali, I., Laks, J., Larsen, S., Mann, J., Mikkelsen, T., Pao, L., Pitter, M., Rettenmeier, A., Sathe, A., Scanzani, F., Schlipf, D., Simley, E., Slinger, C., Wagner, R., and Würth, I.: Remote Sensing for Wind Energy, no. 0029(EN) in DTU Wind Energy E, DTU Wind Energy, Denmark, 2013.

Pielke, R. A. and Panofsky, H. A.: Turbulence characteristics along several towers, Boundary-Layer Meteorology, 1, 115–130, https://doi.org/10.1007/BF00185733, 1970.

670 Pope, S. B.: Turbulent flows, Cambridge University Press, Cambridge and New York, 2000.

Rasmussen, C. E. and Williams, C. K. I.: Gaussian processes for machine learning, Adaptive computation and machine learning, MIT, Cambridge, Mass. and London, 2006.

Ropelewski, C. F., Tennekes, H., and Panofsky, H. A.: Horizontal coherence of wind fluctuations, Boundary-Layer Meteorology, 5, 353–363, https://doi.org/10.1007/BF00155243, 1973.

675 Schlipf, D.: Lidar-assisted control concepts for wind turbines, Dissertation, 2015.

Schlipf, D., Haizmann, F., Cosack, N., Siebers, T., and Cheng, P. W.: Detection of Wind Evolution and Lidar Trajectory Optimization for Lidar-Assisted Wind Turbine Control, Meteorologische Zeitschrift, 24, 565–579, https://doi.org/10.1127/metz/2015/0634, 2015.

Simley, E. and Pao, L. Y.: A longitudinal spatial coherence model for wind evolution based on large-eddy simulation, in: 2015 American Control Conference (ACC), pp. 3708–3714, IEEE, https://doi.org/10.1109/ACC.2015.7171906, 2015.

680 Simley, E., Fürst, H., Haizmann, F., and Schlipf, D.: Optimizing Lidars for Wind Turbine Control Applications—Results from the IEA Wind Task 32 Workshop, Remote Sensing, 10, 863, https://doi.org/10.3390/rs10060863, 2018.

Taylor, G. I.: The Spectrum of Turbulence, Proceedings of the Royal Society A: Mathematical, Physical and Engineering Sciences, 164, 476–490, https://doi.org/10.1098/rspa.1938.0032, 1938.

Veers, P., Powell, D. C., and Connell, J. R.: Three-Dimensional Wind Simulation, 1998.

685 Weitkamp, C.: Lidar: Range-Resolved Optical Remote Sensing of the Atmosphere, vol. 102, Springer-Verlag, New York, https://doi.org/10.1007/b106786, 2005.

Würth, I., Ellinghaus, S., Wigger, M., Niemeier, M. J., Clifton, A., and Cheng, P. W.: Forecasting wind ramps: Can long-range lidar increase accuracy?, Journal of Physics: Conference Series, 1102, 012 013, https://doi.org/10.1088/1742-6596/1102/1/012013, 2018.